Structural, Mechanical, and Tribological Properties of Electrospun Poly(hexamethylene adipamide) Fiber Mats

Matthew M. Mannarino,[a] Reika Katsumata,[b,c] and Gregory C. Rutledge[b,*]

a) Department of Materials Science & Engineering, Massachusetts Institute of Technology, Cambridge, MA 02139
b) Department of Chemical Engineering, Massachusetts Institute of Technology, Cambridge, MA 02139
c) Department of Organic and Polymeric Materials, Tokyo Institute of Technology, Tokyo, Japan

[*] Gregory C. Rutledge
Massachusetts Institute of Technology
77 Massachusetts Ave, Room 66-548
Cambridge MA 02139 USA
Tel.: +1 617 253 0171; fax: +1 617 258 5766.
E-mail address: rutledge@mit.edu

ABSTRACT

The mechanical and tribological properties of electrospun fiber mats are of paramount importance to their utility in a large number of applications. In this work, mats of electrospun fibers of poly(hexamethylene adipamide) (PA 6,6) with average fiber diameter of 238 ± 22 nm are characterized for their crystal structure as well as their mechanical and tribological properties. Post-spin thermal annealing was used to modify the fiber morphology and crystallinity within the fibers. Morphological changes, in-plane tensile response, friction coefficient and wear rate were characterized as functions of the annealing temperature. The mechanical and tribological properties of the thermally annealed PA 6,6 fiber mats exhibited significant improvements through the Brill transition temperature, comparable to the improvements observed for amorphous polyamide electrospun mats annealed near the glass transition temperature. The effective wear rate of the electrospun fiber mats is well-described by a previously proposed modification of the Ratner-Lancaster relationship that relates wear to the yield behavior of these nonwoven mats.

Keywords: Nylon, Electrospinning, Nanofiber, Friction, Wear.

1. Introduction

Electrospinning is a simple yet robust method to create highly porous nonwoven fiber mats from polymeric solutions. In this process, a viscoelastic fluid is charged so that a liquid jet is ejected from the surface of the fluid (typically supplied by a needle or spinneret) and accelerated by an electric field toward a collection electrode, typically a grounded plate. The resulting product is a nonwoven mat composed of fibers with small diameters (~100 nm - 10 μm), high specific surface area (~1-100 m^2/g), and high porosity (~90%) [1,2]. By adjusting the processing and solution parameters, the fiber diameter, porosity, specific surface area and mechanical properties of the mat can be tailored for various applications. The unique properties and relative ease of fabrication of electrospun fibers and their nonwoven mats have led to their use in a broad range of applications [3,4] including (but not limited to): degradable biomedical scaffolds [5,6], optical sensors [7], and ion-exchange membranes [8,9]. In each of these applications the mechanical and tribological response of the fiber mat is critical to the utility of the device.

Individual electrospun fibers have been shown to exhibit some remarkable increases in elastic stiffness and yield stress below a critical, submicrometer diameter, the value of which has been found to vary from polymer to polymer [10,11]; however, the origin of these increases in single fiber mechanical properties remains a topic of some debate, and may differ depending on the polymer. For non-crystalline fibers like those formed from poly(trimethyl hexamethylene terephthalamide) (PA 6(3)T), an amorphous nylon, the increases in stiffness and yield stress have been shown conclusively to result from increased molecular orientation, which in turn was attributed to increased strain during formation [11]. Regardless of the diameter-dependent changes in fiber properties, the as-spun mats tend to exhibit consistently low yield stresses (typically 0.5-3 MPa), Young's moduli (typically 20-60 MPa) and toughnesses (typically 0.5-2 MJ/m^3) [12,13]. For some applications such as tissue engineering, where a soft, porous matrix is desirable, this may be an advantage; however, for many applications of nonwoven mats, notably membranes and textiles, for example, modest improvements to the mechanical integrity without significant losses in the inherently high porosity or specific surface area would be highly desirable. Although many experimental studies have been conducted on the mechanical properties of conventional nonwoven fabrics, there are a limited number of reports that account adequately for the observed mechanical properties of mats comprising electrospun fibers [14,15]. In recent years several research groups have demonstrated significant improvements to the Young's modulus and yield stress of electrospun polymeric fiber mats by various forms of post-spinning techniques such as thermal annealing [16,17], mechanical drawing [18], hot pressing [19], and solvent vapor treatment [20]. For amorphous polymer nonwovens, thermal annealing has been shown to consolidate the fibers, creating stronger, more uniform materials [21]. In addition, if the amorphous polymer fiber mats are annealed above the material's glass transition temperature (T_g), flow and welding between fibers can be observed, which enhances mechanical properties through the mechanism of increased number (and perhaps rigidity) of junctions.

For a broad range of applications, nonwoven fiber materials must be not only strong, but also wear-resistant. Derler et al. have measured the friction coefficient and hardness of conventional textiles in contact with human skin equivalents [22]. Gerhardt et al. have measured the frictional properties and contact pressure of skin-fabric interactions [23]. The textile industry currently uses several abrasion and wear testing techniques (such as the Taber abraser) to evaluate the durability of fabrics. Such tribological characterization is necessary for electrospun fiber mats as well, if they are to be developed and commercialized. We have recently reported the first quantitative study of friction and wear resistance for electrospun fiber mats of the amorphous nylon PA 6(3)T. We showed that wear correlates well with the yield properties of the nonwoven mat, in accord with a modified Ratner-Lancaster model, and that significant improvements can be realized by thermal annealing in the vicinity of the polymer glass transition [17]. Here, we report the study of friction and wear resistance for electrospun fiber mats of the semicrystalline nylon, poly(hexamethylene adipamide) (PA 6,6). The crystal structure and polymorphic phase transitions within electrospun Nylon 6 and Nylon 6,6 fibers have been previously investigated [24,25], as have the tensile mechanical properties of the electrospun Nylon 6,6 fibers [25]. Subjecting a semi-crystalline polymer fiber to heat treatment at a temperature above the crystallization temperature (T_c) of that polymer, but below the equilibrium melting temperature (T_m) can cause the melting of small, imperfect crystals, and the formation of larger, more perfect crystals within the fibers, thus creating a stiffer and tougher matrix [26,27]. The effect of crystallinity on the tribological properties of electrospun nonwoven mats has, to our knowledge, not yet been reported. This work reports the tribology of semi-crystalline PA 6,6 electrospun mats, correlates this with mechanical properties, and demonstrates the improvement of both mechanical integrity and wear resistance by post-spin annealing, to generate more robust membranes.

2. Experimental

2.1. Materials

Poly(hexamethylene adipamide) (Nylon 6,6), henceforth referred to as PA 6,6, was purchased from Scientific Polymer Products, Inc. It is a semi-crystalline polyamide with a glass transition temperature of 45 °C (T_g=318 K) and crystal melting temperature of 254 °C (T_m=527 K) as reported by the vendor and confirmed by differential scanning calorimetry. N,N-dimethyl formamide (DMF) and formic acid (FA) were purchased from Sigma-Aldrich and used as received to create solutions with the composition 20:75:5 by weight of PA 6,6:FA:DMF. The less volatile DMF was added to prevent solidification of the solution at the needle tip and to decrease the solution conductivity.

2.2. Electrospinning of Fiber Mats

Fiber mats were fabricated by electrospinning from organic polymer solutions using a parallel plate geometry inclined at 45° with respect to vertical, as shown in Figure 1. Two aluminum plates (the top one 12 cm in diameter, the bottom one a 20 cm square plate) were positioned as illustrated with a tip-to-collector distance of 20 cm. The rotated geometry of the electrospinning process was employed to avoid dripping of solution onto the electrospun fiber mats, which re-dissolves the PA 6,6 fibers and disrupts the uniform fiber matrix morphology; the change in orientation should have no effect on the physics of fiber formation. A high voltage power supply (Gamma High Voltage Research, ES40P) was used to apply an electrical potential of 28 kV to the polymer solution and the top plate. The nozzle consisted of a stainless steel capillary tube (1.6 mm OD, 1.0 mm ID) (Upchurch Scientific) in the center of the top plate. A digitally controlled syringe pump (Harvard Apparatus, PHD 2000) was used to obtain a constant flow rate of 0.0023 mL/min. The entire apparatus was contained within a fume hood to ensure proper ventilation. PA 6,6 is well known to be hygroscopic, and the spinning process was found to be very sensitive to humidity. All samples fabricated for testing in this work were collected between 15-25% relative humidity (RH) and stored after fabrication in a sealed dry box, containing desiccant to remove any atmospheric moisture. An anti-stick agent (CP Fluoroglide® from Saint-Gobain Performance Plastics) was sprayed onto the aluminum collector plate to facilitate removal of the electrospun mat. Each mat of approximately 11-12 cm in diameter and 100 μm in thickness was produced from 0.5 mL of PA 6,6 solution.

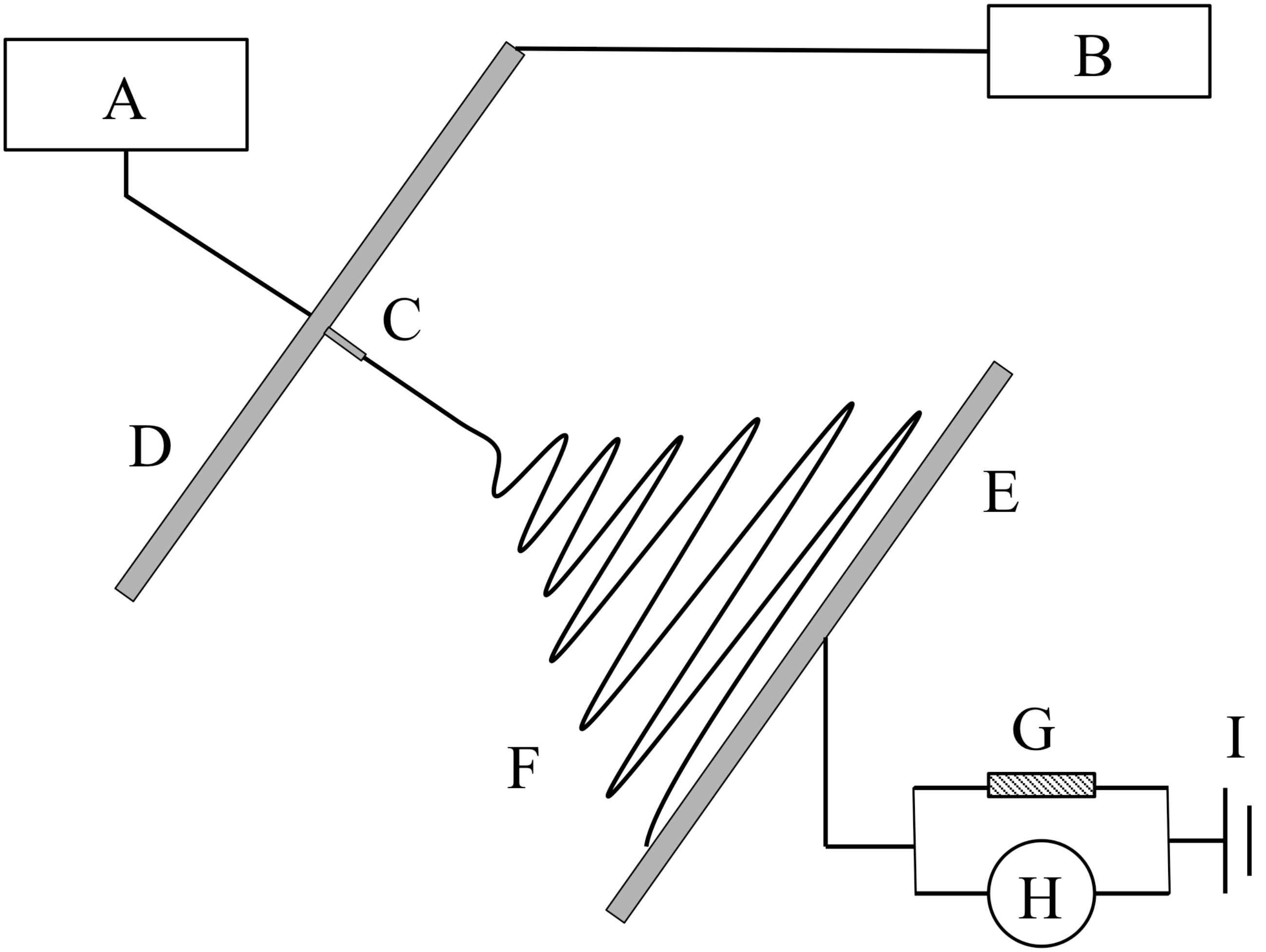

Figure 1. Schematic representation of 45°-rotated parallel-plate electrospinning apparatus: (A) solution pump; (B) high voltage power supply; (C) capillary tip; (D) upper plate; (E) lower grounding collector plate; (F) whipping polymer fiber jet; (G) resistor; (H) voltage meter; (I) ground.

2.3. Morphological Characterization of Fiber Mats

A JEOL JSM-6060 scanning electron microscope (SEM), with an accelerating voltage of 10-15 kV and a working distance of 10 mm, was used to determine the diameter and morphology of the fibers. A thin layer (~10 nm) of gold was sputter-coated onto SEM samples prior to imaging. The mean and standard deviation of fiber diameter were determined based on 100 measurements of fiber diameter from a set of SEM micrographs at 17,000X magnification using ImageJ. Porosity of the fiber mats was determined gravimetrically by cutting out rectangular sections and measuring the mass and dimensions of the mat specimen and converting to porosity. Five mat thickness measurements were taken per sample with a Mitutoyo digital micrometer with a constant measuring force of 0.5 N; the mean thickness was used for porosity calculations. Lateral sample dimensions were determined using a digital caliper with 0.01 mm precision. The volume and mass of the specimen were then converted to a porosity using the bulk density of PA 6,6 (1.14 g/cm^3 for the amorphous nylon; 1.25-1.30 g/cm^3 for specimens of 40-60 % crystallinity) and the following equations [28,29],

$$\rho_{app} = \frac{m_{mat}}{h_{mat} \times A_{mat}} \tag{1}$$

$$\phi = \left(1 - \frac{\rho_{app}}{\rho_{bulk}}\right) \times 100\% \tag{2}$$

where ρ_{app} is the apparent density, m_{mat} is the mass of mat, h_{mat} is the thickness of mat, A_{mat} is the area of mat, ϕ is the mat porosity (%) and ρ_{bulk} is the bulk density.

2.4. Thermal Annealing of Electrospun Mats

The electrospun mats were thermally annealed in a Thermolyne lab oven. Each mat was draped over a 100 mm diameter pyrex dish and placed in the oven for 60 minutes at a specified temperature. Nitrogen was introduced during annealing at 240 and 270 °C to prevent degradation and charring of the PA 6,6. Contact of the mat with the rim of the pyrex dish was sufficient to prevent the mats from tearing during heat treatment and suspended the sample so that it did not contact or stick to any surfaces. After annealing, samples were removed from the oven and allowed to cool before carefully cutting the mat off of the pyrex dish.

2.5. Crystal Structure Analysis

Differential scanning calorimetry (DSC) was performed using a TA Instruments Discovery Series DSC Model 972001. Samples of 4-6 mg were prepared in standard aluminum pans and equilibrated in the DSC under nitrogen purge for 5 minutes at 40 °C before being ramped up to 295 °C at 10 °C/min to determine the crystallinity. Samples were then held isothermally at 295 °C for 5 minutes before ramping back down to 40 °C at 10 °C/min to confirm the crystallization temperature (T_c) of the PA 6,6 samples. TRIOS software version 2.5.0 was used to analyze the DSC data. Crystallinity was calculated from the heat absorbed in the melting endotherm and the heat of fusion of PA 6,6 ($\Delta H°=191.9$ J/g) [30].

Wide-angle X-ray diffraction (WAXD) patterns were obtained using a Molecular Metrology ASSY 610 X-ray diffractometer at 45 kV and 0.66 mA. The distance between the detector and the sample for WAXD was 117 mm. The wavelength of the X-ray beam (Cu-K$_\alpha$) was $\lambda=1.54$ Å, and the beam was aligned and calibrated using a silver behenate standard with the first reflection peak at the scattering vector $q=(4\pi\sin\theta)/\lambda)=1.076$ nm^{-1}, where θ is the scattering half-angle. Fuji imaging plates were used as X-ray detectors with a typical exposure time of 6 hours. Digital WAXD images were obtained using a Fuji BAS-1800II scanner and analyzed using Polar® X-ray Diffraction (XRD) analysis software version 2.7.5, with a Voigt peak-fitting model to deconvolute the crystalline and amorphous regions and determine the percent crystallinity.

Polarized infrared spectra were measured using a Nicolet 6700 Fourier transform infrared (FT-IR) spectrometer equipped with a Nicolet Continuum infrared microscope (Thermo Fisher Scientific, Waltham, MA). An IR polarizer was used in transmission mode, and 128 scans were recorded in the range of wavenumber from 650 to 4000 cm^{-1} for polarization both parallel and perpendicular to the fiber axis. Bundles of aligned fibers were collected as described previously and used for FTIR, due to limitations in sensitivity of the instrument to measure single fibers [11]. OMNIC software was used to analyze the FTIR spectra. The dichroic ratio was used to characterize crystal orientation; it is defined as $D=A_{\|}/A_{\perp}$, where $A_{\|}$ and $A_{\perp}$ are the absorbances measured with the incident beam polarized parallel and perpendicular to the fiber bundle axis, respectively. The dichroic ratio can be related to an orientation function, f [11,31]:

$$f = \frac{(D-1)/(D+2)}{(2\cot^2\alpha-1)/(2\cot^2\alpha+2)} \tag{3}$$

where α is selected to be the angle between the molecular axis and the transition moment vector of the CH_2 twist-wagging mode around 1200 cm^{-1} in PA 6,6 (α=0°) [32]. The orientation function, f, is related to the second moment of molecular orientation $\langle\cos^2\theta\rangle$ by the expression

$$f = [3\langle\cos^2\theta\rangle - 1]/2 \tag{4}$$

where $f = 1$ corresponds to perfect uniaxial alignment of molecules in the fiber direction, $f = 0$ corresponds to the absence of preferred molecular orientation, and $f = -1/2$ corresponds to molecular alignment perpendicular to the fiber axis.

2.6. Mechanical Testing

Uniaxial tensile testing of electrospun fiber mats was performed with a Zwick Roell Z2.5 tensile testing machine using a 2.5 kN load cell. Rectangular specimens were cut to 50 mm × 12 mm and extended at a constant extension rate of 0.36 mm/s with a 36 mm gauge length (corresponding to a strain rate of 0.01 s^{-1}). Five specimens were tested for each temperature of thermal treatment to determine the mean and standard deviation. The thickness of each specimen was determined from the average of three measurements taken along the gauge length with a Mitutoyo digital micrometer with a constant measuring force of 0.5 N. The force–displacement data was converted to engineering stress versus engineering strain results using the initial thickness, width and gauge length of the test specimen. Young's modulus was determined from the maximum slope of the engineering stress-engineering strain curve in the elastic region. Yield stress was determined from the intersection of the linear fit to the elastic deformation region at small strain with a linear fit to the plastic deformation region at large strain.

2.6. Tribological Testing

The coefficient of friction was measured according to ASTM D-1894-11 [Standard Test Method for Static and Kinetic Coefficients of Friction of Plastic Film and Sheeting] using a custom-made “sled and spring gauge” apparatus. Friction force measurements were taken with a series of normal forces ranging from 0.5-2.5 N with an IMADA push-pull force gauge (10 N capacity and 0.05 N precision), at a testing speed of 0.25 m/s. Five measurements were taken for each set of heat-treated mats to determine the mean and standard deviation. The counter-face used for coefficient of friction measurements was the H-38 Calibrade® standardized abrasion testing wheel used in the abrasive wear testing experiments.

The surface roughness of the fiber mats and polymer film were measured using a Veeco surface profiling system, Model “Dektak 150”. A 2.5 μm stylus with 3.0 mg tip force was used to scan across 5.0 mm of sample in 30 seconds. The arithmetic average roughness (R_a) was recorded for each sample analysis, and the average of five scans was used to determine the mean R_a.

The abrasive wear resistance of the electrospun mats was measured by a modified ASTM D-3884-09 [Standard Test Method for Abrasion Resistance of Textile Fabrics (Rotary Platform, Double-Head Method)], similar to the method outlined in [17]. Test samples were prepared by carefully cutting out 100 mm diameter circles from an electrospun mat and attaching them to the adhesive side of a 100 mm diameter Polyken® 339 duct closure foil. This prevents the mats from bunching up or shifting during testing. Five 100 mm specimens were prepared for each combination of annealing temperature and specified number of abrasion cycles, to determine the mean and standard deviation. H-38 Calibrade® standardized abrasion testing wheels were used with an applied load of 50 g for 10, 50, 100, 250, and 500 cycles at 1 revolution per second (25 cm/s). The H-38 Calibrade® standardized Taber abrasion wheel is classified in ASTM D-3884-09 as a very fine-grained abrasive wheel for use in testing woven and nonwoven fabrics as well as delicate textiles. Samples were conditioned overnight in a sealed box, containing desiccant, to remove any residual atmospheric moisture from the fibers, since moisture is known to affect the mechanical properties of polyamides [33,34]. Abrasive wear testing was conducted entirely within a sealed glove box maintained at <1% RH with a dry air purge, in order to prevent the absorption of water that would disrupt the mass-loss measurements. The temperature of the electrospun mats was monitored during testing using an OSXL450 non-contact infrared thermometer to ensure that there was not a significant amount of frictional heating during the course of abrasive wear testing. Samples were analyzed for abrasive wear by visual inspection and mass loss using an Ohaus E11140 analytical balance. By measuring the mass loss of the fiber mats after a specified number of cycles (or sliding distance), the effective wear rates of the membranes were determined. The data for mass loss vs. number of cycles for each sample were fitted to a second order polynomial forced through the origin, using the method of least squares. An effective wear rate for each sample was then calculated by taking the value of the tangent to the second order polynomial at 100 cycles.

3. Results and Discussion

3.1 Morphology/Porosity of Heat-Treated PA 6,6 Mats

Uniform PA 6,6 fibers having a mean diameter of 238 ± 22 nm were fabricated from a 20 wt% solution in 15:1 FA:DMF for use in all of the tests described here. Each nonwoven fiber mat was produced using 0.5 mL of polymer solution to generate a mat of roughly 100 µm thickness and 12 cm in diameter. The mats were then annealed at one of several temperatures selected to bracket the major thermal transitions of PA 6,6: T_g (45 °C), T_c (240 °C), and T_m (254 °C). PA 6,6 also exhibits a broad thermal transition between 80 and 170 °C called the Brill transition, T_B. It is believed that the thermal annealing serves to drive out any residual solvent or air pockets within the fibers, increase the number of weld points between fibers, and alter the crystal morphology and crystalline fraction. Figure 2 shows SEM micrographs of PA 6,6 fibers after 1 hour of annealing at various temperatures. There are no discernable weld points between fibers on the untreated SEM, nor are there any observable morphological changes for the 70 °C annealed sample; however at 170 °C and 240 °C thermal treatment, several weld points become visible, as well as some qualitative densification of the fiber mat. The 270 °C annealed PA 6,6 fiber mat exhibits extensive flow and fusion between fibers, leading to considerable loss of the original fiber morphology and porosity, thus creating a webbing effect between fibers similar to that seen previously in the thermal annealing of an amorphous polyamide above T_g [17].

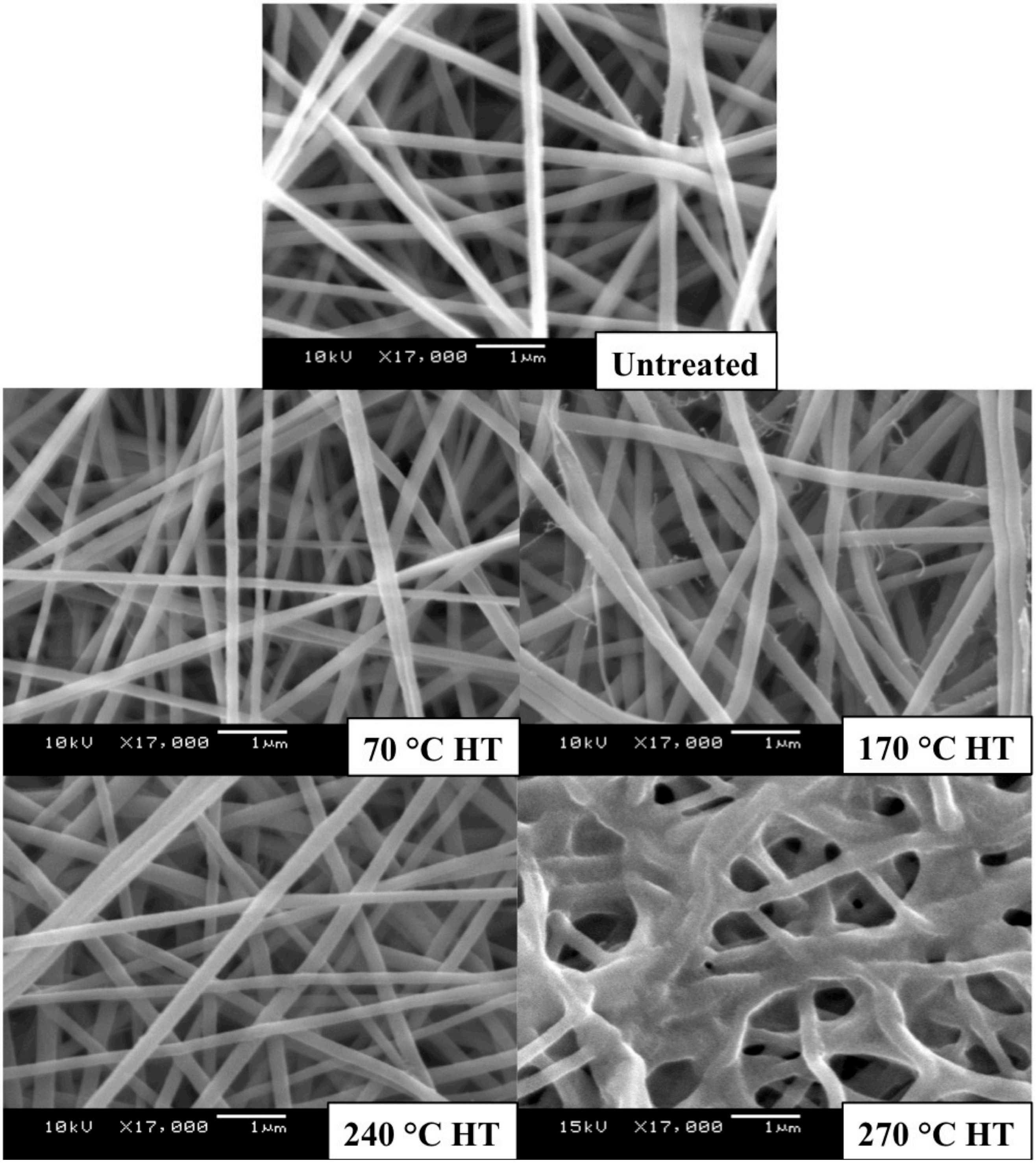

Figure 2. SEM micrographs of untreated electrospun PA 6,6 nanofibers (left), and after 60 minutes of thermal treatment at 70, 170, 240, and 270 °C. Scale bar for all images is 1 μm. HT refers to the heat treatment (annealing) temperature.

The SEM micrographs indicate that there may be a decrease in the pore size between fibers as the temperature of annealing increases, as well as what appears to be a decrease in the overall porosity of the mats. Before the mats were subjected to the heat-treatment, they were typically 100 ± 10 μm in thickness. At the highest annealing temperature (270 °C), the mats were observed to contract to as thin as 55 ± 10 μm, while maintaining a fixed diameter of 100 mm. Figure 3 shows the results for porosity of electrospun PA 6,6 fiber mats after annealing at each temperature. The nonwoven mats have an inherently high as-spun porosity of 90.8 ± 1.4%, which drops slightly to 86.8 ± 1.0% as the result of the 170 °C heat treatment (between the T_g and T_c). Annealing at temperatures above the T_m produces a more significant drop in porosity, falling to 72.1 ± 2.6%, which is consistent with the significant changes observed in the SEM micrographs from Figure 2.

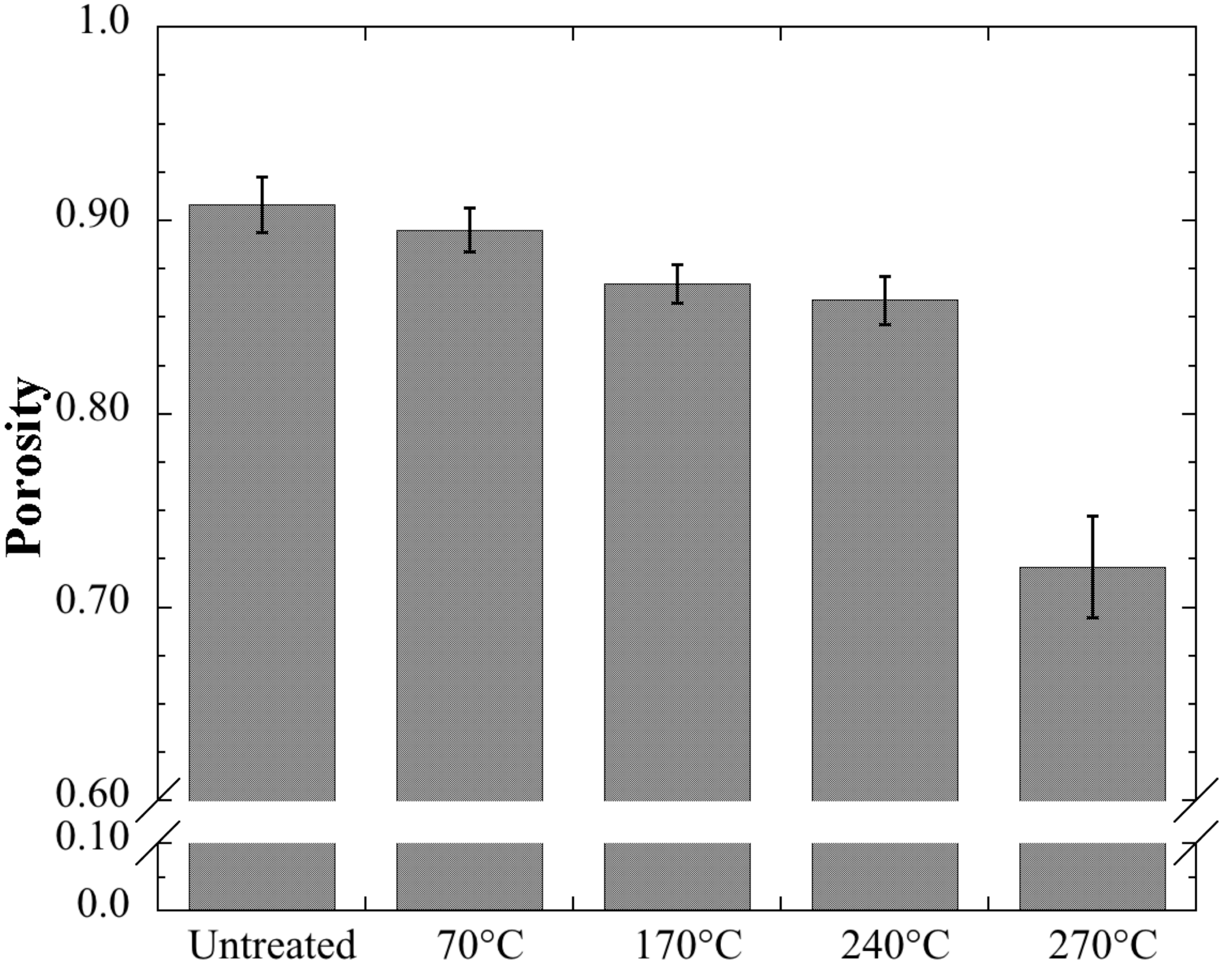

Figure 3. Porosity of PA 6,6 nanofiber mats after thermal annealing at various temperatures.

3.2. Crystal Structure of Annealed PA 6,6 Fibers

The crystalline structures of PA 6,6 electrospun fibers were characterized by WAXD at room temperature for each annealing temperature. The azimuthally-integrated WAXD profiles of the annealed PA 6,6 fiber samples are plotted in Figure 4; the plots show broad scattering regions for the as-spun and

70 °C HT samples and two distinct narrow scattering peaks for the samples annealed at 240 °C and 270 °C. The sample annealed at 170 °C HT exhibits a scattering pattern intermediate between these two extremes. The as-spun PA 6,6 fiber mat exhibits a relatively strong (100) diffraction peak at a 2θ scattering angle of 20.2 degrees, and a second broader (010)/(110) doublet diffraction peak at a 2θ of 23.0 degrees, corresponding to the triclinic α crystal structure of PA 6,6 [35,36]. Consistent with previous reports, the diffraction peak are relatively broad, indicating that the sizes of PA 6,6 crystallites are small and heterogeneous in the electrospun fibers [24]. The sample annealed at 70 °C shows a shift of the diffraction peaks to 20.9 and 23.6 degrees, with a corresponding loss of intensity, suggestive of some melting out of the least stable crystallites. Meanwhile, the sample annealed at 170 °C HT also exhibits broad, low intensity peaks, but these are shifted back to 20.4 and 22.8 degrees, with both the (100) and (010)/(110) diffraction peak intensities closer in magnitude to each other; this behavior is consistent with transformation of the triclinic α form to a pseudo-hexagonal form above the Brill transition temperature, followed by recovery of the triclinic form upon cooling [36,37,38,39]. The samples annealed at 240 °C and 270 °C exhibit very similar WAXD profiles, but with higher intensity. This is a consequence of the fact that both are cooled following annealing well above T_B. These samples each exhibit a new, small (002) peak at a 2θ of 13.9 and 14.1 degrees, very sharp (100) diffraction peaks at a 2θ of 20.0 and 20.2 degrees, and an additional sharp (010)/(110) doublet diffraction peak at a 2θ of 23.4 and 23.5 degrees, respectively. Sharper peaks (and larger crystallites) are achieved through thermal annealing of the PA 6,6 fiber mats between T_B and T_m.

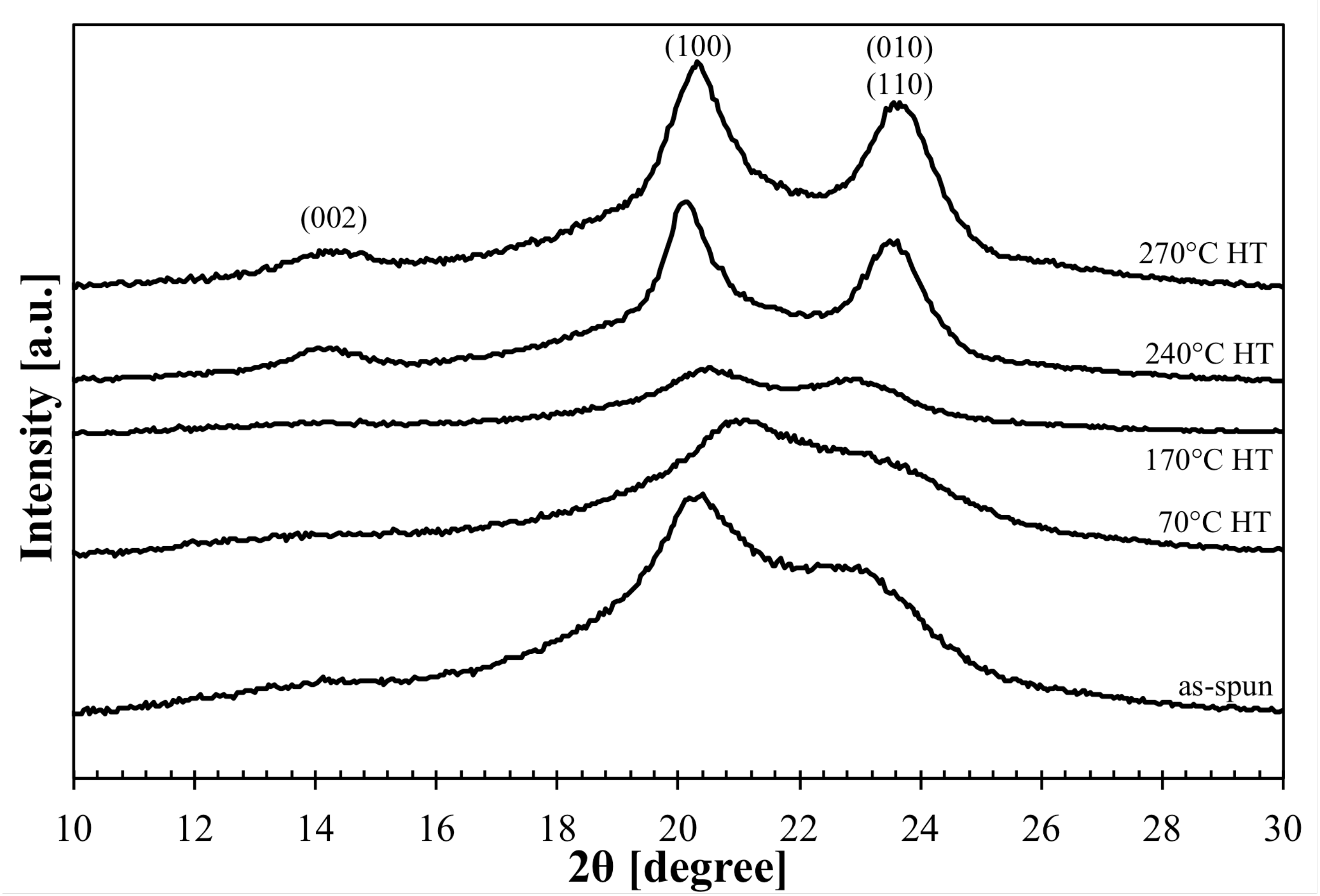

Figure 4. WAXD profiles of electrospun PA 6,6 fiber mats: as-spun, 70°C HT, 170°C HT, 240°C HT, and 270°C HT. HT refers to the heat treatment (annealing) temperature.

Polarized IR absorption was used to measure the dichroism of the peak around 1200 cm^{-1}, which is attributed to the CH_2 twist-wagging vibration mode in the α-crystalline phase of PA 6,6 [35,40]. Polarized FTIR spectra for the oriented PA 6,6 fiber bundles at each annealing temperature are shown in Figure 5. The solid lines represent the absorbance perpendicular to the fiber axis, $A_{\perp}$, indicative of alignment of the PA 6,6 backbone parallel to the fiber axis, and the dotted lines represent the absorbance parallel to the fiber axis, $A_{\parallel}$, indicative of molecular alignment perpendicular to the fiber axis Visual inspection of the polarized FTIR spectra indicate that the samples annealed below the T_m of PA 6,6 all exhibit a greater absorbance of CH_2 twist-wagging parallel to the fiber axis, while the two samples treated near or above T_m, exhibit higher absorbance perpendicular to the fiber axis. Values for the dichroic ratio and orientation function of PA 6,6 fiber bundles are tabulated in Table 1. The orientation function value for the as-spun sample is 0.054, indicating some preferential crystal orientation parallel to the fiber axis. There is a modest increase in f for the 70 °C and 170 °C heat-treated samples to 0.109 and 0.074 respectively. When annealed above T_B, the calculated value of f drops below 0, to -0.099 for the sample annealed at 240 °C, and even further to -0.181 for the sample annealed at 270 °C. This transition of the molecular orientation function from slightly positive (oriented along fiber axis) to slightly negative (oriented perpendicular to fiber axis) indicates significant changes to the crystal organization within the fibers occur when annealed above the crystal Brill transition temperature.

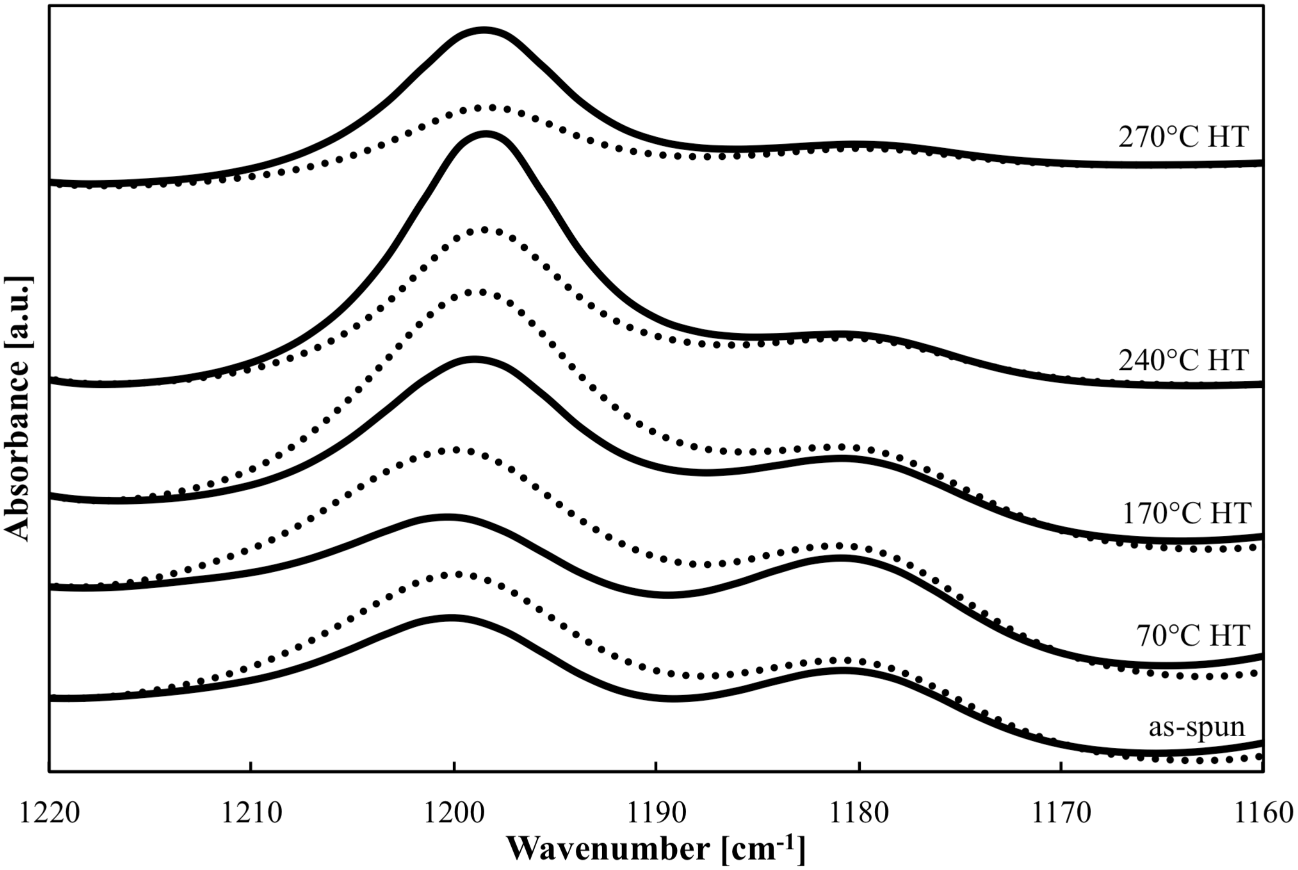

Figure 5. Polarized FTIR of oriented PA 6,6 fiber bundles after annealing at various temperatures. Solid lines represent $A_{\perp}$ and dotted lines represent $A_{\parallel}$.

Thermal heating profiles of the electrospun PA 6,6 fiber mats were obtained by DSC. The first heating at 10 °C/min was used in order to determine the T_m of the PA 6,6 crystals as well as the heat required to melt the crystalline regions of the polymer; the first cooling was used to confirm the T_c of the PA 6,6 samples (240 °C), and did not change significantly with temperature of annealing. Figure 6 shows the first heating thermal profiles from 40 °C to 295 °C for each of the annealed electrospun PA 6,6 mat samples (solid lines), and a typical first cooling profile for the as-spun sample (dotted line). The as-spun sample exhibits a broad melting peak with a T_m of 255.8 °C for the fibers crystallized from solution; this is very close to the reported value from the manufacturer (254 °C). The samples annealed at 70 °C and 170 °C exhibit melting peaks with a similar breadth; however, the peaks are split into two distinct melting points: 252.6 °C and 254.4 °C, respectively, for the first melting peak, and 257.1 °C and 259.2 °C for the second melting peak, which we interpret as indication of cold crystallization within the fibers. The sample annealed at 240 °C exhibits a significant change in the heating profile, with a large shift in the first melting peak to 237.5 °C (close to the annealing temperature of 240 °C), and a second smaller melting peak at 247.8 °C. This shift in the melting peak indicates that the thermal treatment at 240°C (above the T_B of PA 6,6) leads to substantial melting and recrystallization within the fibers. The sample annealed at 270 °C exhibits a broad melting peak with a single T_m of 253.0 °C, indicating that the sample readily recrystallized during the quench after annealing; however, the heat required to melt the crystallites of the 270 °C was lower than that for any other sample, indicating that some melting of crystallites did take place at this temperature and was not recovered.

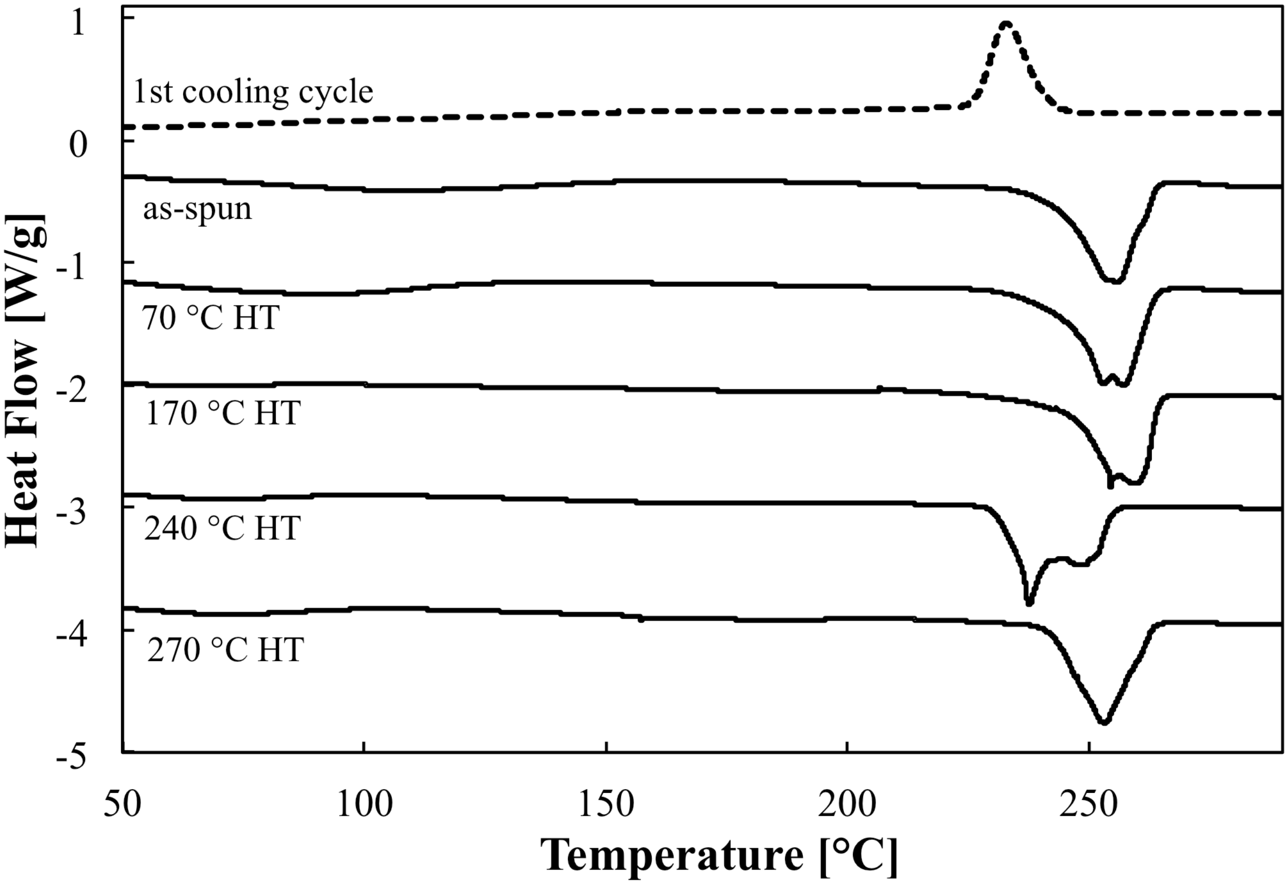

Figure 6. DSC Thermographs of electrospun PA 6,6 fiber mats from the first heating: as- spun, 70°C HT, 170°C HT, 240°C HT, and 270°C HT (solid lines); also shown is a typical first cooling cycle for the as-spun fiber mat (dotted line).

A summary of the thermal properties and crystal structure analysis of the electrospun PA 6,6 fiber mats is shown in Table 1. The percent crystallinity, as measured from WAXD, was determined by deconvoluting the crystalline and amorphous regions of the 1D-integrated intensity profiles using Polar analysis software and then normalizing the area under the crystal peaks by the total integrated intensity. Percent crystallinity, as determined by DSC, was calculated based on the integrated area of the melting endotherm divided by the heat of fusion of 191.9 J/g for an ideal α-form PA 6,6 crystal [30]. The percent crystallinities of the PA 6,6 fibers determined by WAXD and DSC exhibited differing values and trends. The percent crystallinity of the PA 6,6 fiber mats, as calculated from deconvolution of the WAXD spectra, decreases from 38.8% for the as-spun sample to 34.9% and 35.7% for the 70 °C and 170 °C heat-treated samples, respectively. Thermal annealing above T_B showed an increase in the percent crystallinity to 40.1% for the 240 °C annealed sample and 44.9% crystallinity for the 270 °C thermally annealed sample. The percent crystallinity as measured by DSC, showed the as-spun fibers to be 41.0% crystalline, while the samples annealed at 70 °C exhibited a small drop to 40.1%, indicating that the annealing temperature was too low to cause significant changes to the crystal structure of the polymer. The crystallinity dropped more significantly, to 34.4%, for the samples annealed at 170 °C, and an even further to 32.7% for the samples annealed at 240 °C. These results show that while the annealing process changes the crystal structure of the PA 6,6 fibers, the total percent crystallinity of the samples also changes with temperature of thermal treatment. The relatively high percent crystallinity for the 270 °C (44.9% by WAXD) confirms that the annealing and subsequent quenching process of the fiber mats produced larger, but perhaps less perfect, crystallites.

Table 1. Structural Properties of Heat-treated Electrospun PA 6,6 Fiber Mats

Sample	**D**	***f***	**Crystallinity (WAXD) [%]**	**Crystallinity (DSC) [%]**	**T_m (DSC-1st Peak) [°C]**	**T_m (DSC-2nd Peak) [°C]**
As-spun	1.17	0.054	38.8	41.0	255.8	-
70 °C HT	1.37	0.109	34.9	40.1	252.6	257.1
170 °C HT	1.24	0.074	35.7	34.4	254.4	259.2
240 °C HT	0.73	-0.091	40.1	32.7	237.5	247.8
270 °C HT	0.54	-0.181	44.9	32.2	253.0	-

3.3. Mechanical Properties of Heat-Treated Mats

Uniaxial, constant strain-rate tensile testing was employed to observe the effect of the annealing temperature on the mechanical response of the semi-crystalline electrospun fiber mats. Representative plots of the tensile behavior of heat-treated electrospun mats are shown in Figure 7; note the slight increase in modulus and yield stress with increasing temperature of heat-treatment and the transition from more highly extensible, plastic behavior for the untreated sample to more brittle behavior when annealing close to or above T_m. The PA 6,6 mats as-spun and annealed at 70 °C both exhibited the most ductile behavior, with large plastic deformation regions extending well beyond 50% breaking strain for most of the samples tested. The samples annealed at 170 °C and 240 °C exhibited some ductility, with higher elastic moduli, and breaking strains of 35-45%. The sample annealed at 270 °C exhibited much more brittle behavior, with a very narrow plastic deformation region, breaking very shortly after reaching the yield point. This behavior is similar to that observed for the amorphous nylon electrospun fiber mat annealed above T_g [17].

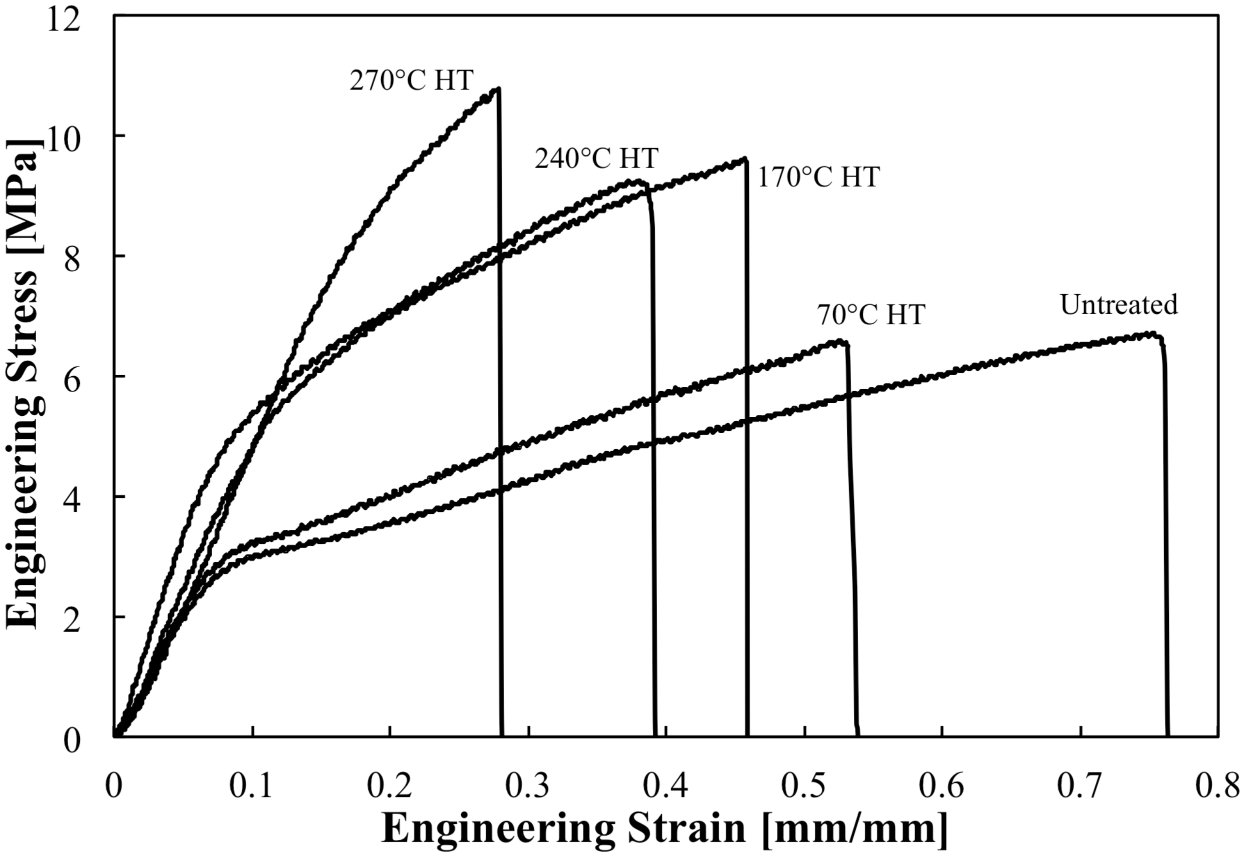

Figure 7. Representative stress-strain curves for PA 6,6 fiber mats as-spun and after annealing at various temperatures (1 hour each at 70, 170, 240, and 270 °C).

Analysis of the nonwoven mat tensile testing results show that thermal annealing of the electrospun fiber mats can significantly alter their mechanical properties. Plots showing changes to the Young's modulus, yield stress, maximum (breaking) stress, breaking strain, and tensile energy-to-break (toughness) are plotted in Figures 8-10. The Young's modulus for the as-spun material was 45.11 ± 2.30 MPa and did not increase when thermally annealed slightly above T_g (70 °C HT sample); however, it did increase modestly to 67.81 ± 6.53 MPa after annealing at 170 °C (between T_g & T_m), as shown in Figure 8. Further improvements to the Young's modulus were not observed in the samples annealed around the T_m of PA 6,6 (240 °C and 270 °C), indicating that crystal annealing/melting within the fibers does not have a significant effect on the Young's modulus of the nonwoven mat.

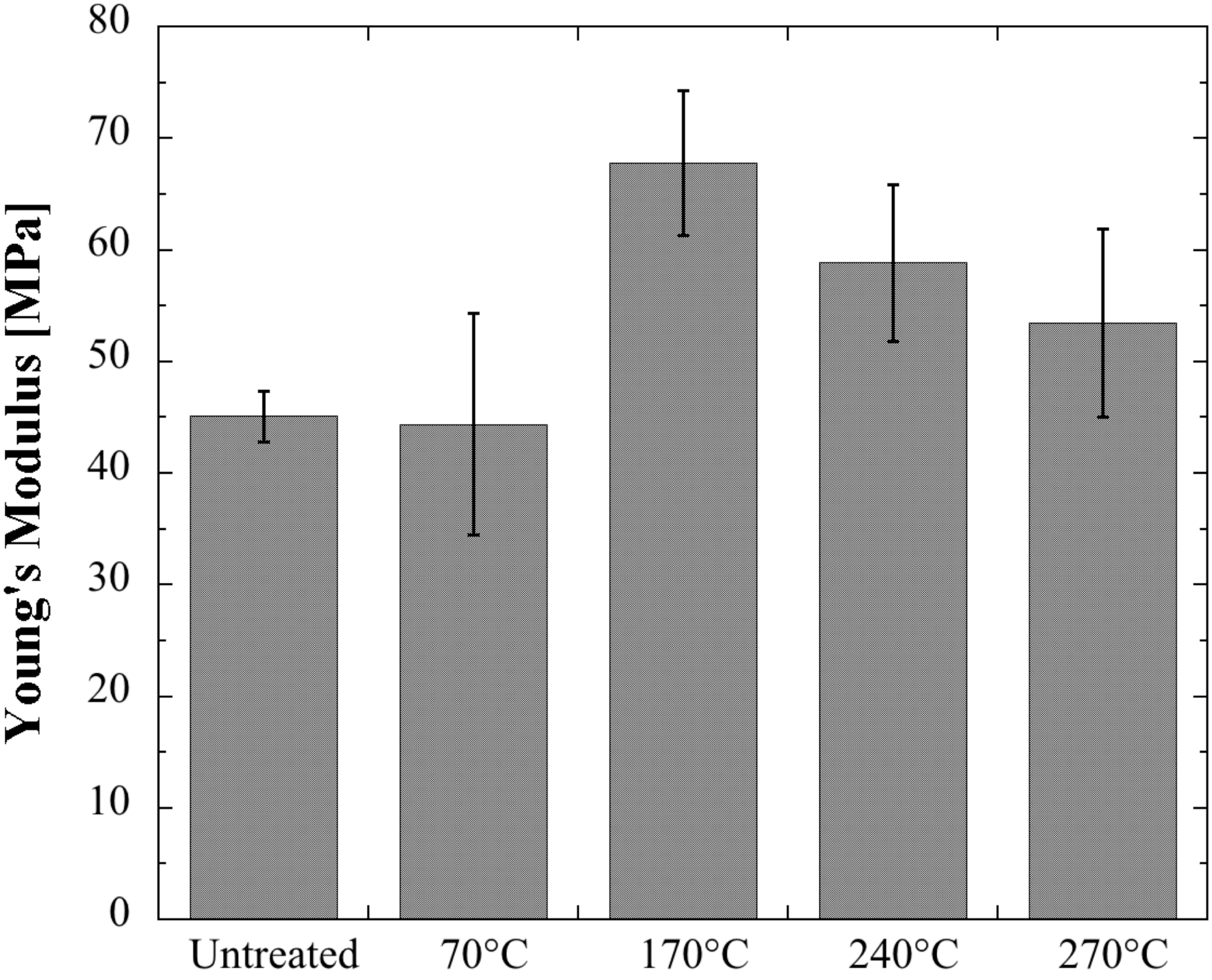

Figure 8. Plot of Young's modulus vs. annealing temperature for PA 6,6 nanofiber mats.

The yield stress and maximum (breaking) stress of the mats as a function of annealing temperature is shown in Figure 9. Steady increases in the yield stress are observed from the as-spun state at 2.92 ± 0.14 MPa up to 4.54 ± 0.43 MPa for the samples annealed above T_g (170 °C), then increases even further for samples annealed above T_m (7.05 ± 1.10 MPa for the 270 °C HT). The bar graph for the yield stress looks very similar to the inverse of the trend in porosity shown in Figure 3, with consistent increases in the yield stress for each increase in the temperature of annealing. The maximum (breaking) tensile stress of the PA 6,6 mats shows a modest increase between 70 °C and 170 °C thermal treatment (increasing from 5.94 ± 0.99 MPa to 9.03 ± 1.37 MPa); however, no further increases in the breaking stress is observed with annealing at higher temperatures than 170 °C, and all values are statistically identical for samples annealed at 170, 240, or 270 °C.

Bar graphs for strain at break and for toughness of the electrospun fiber mats are shown in Figure 10. They do not follow a consistent trend with increasing annealing temperature. There is a slight drop in the strain at break for the sample annealed at 170 °C and another drop for the sample annealed at 240 °C, indicating a possible transition from a ductile fracture response to more brittle behavior or introduction of microstructural flaws or stress concentrators (crystallites) causing premature fracture. The toughness of the electrospun mats correlates very closely to the strain at break. This behavior reflects the fact that the breaking stress for all of the samples did not vary by more than 50% from the lowest mean value to the highest, while the strain to break dropped from 0.67 ± 0.11 mm/mm to 0.27 ± 0.05 mm/mm for the as-spun sample and the sample annealed at 270 °C, respectively. This suggests that the breaking strain is the dominant factor in determining the tensile energy-to-break for the PA 6,6 fiber mats.

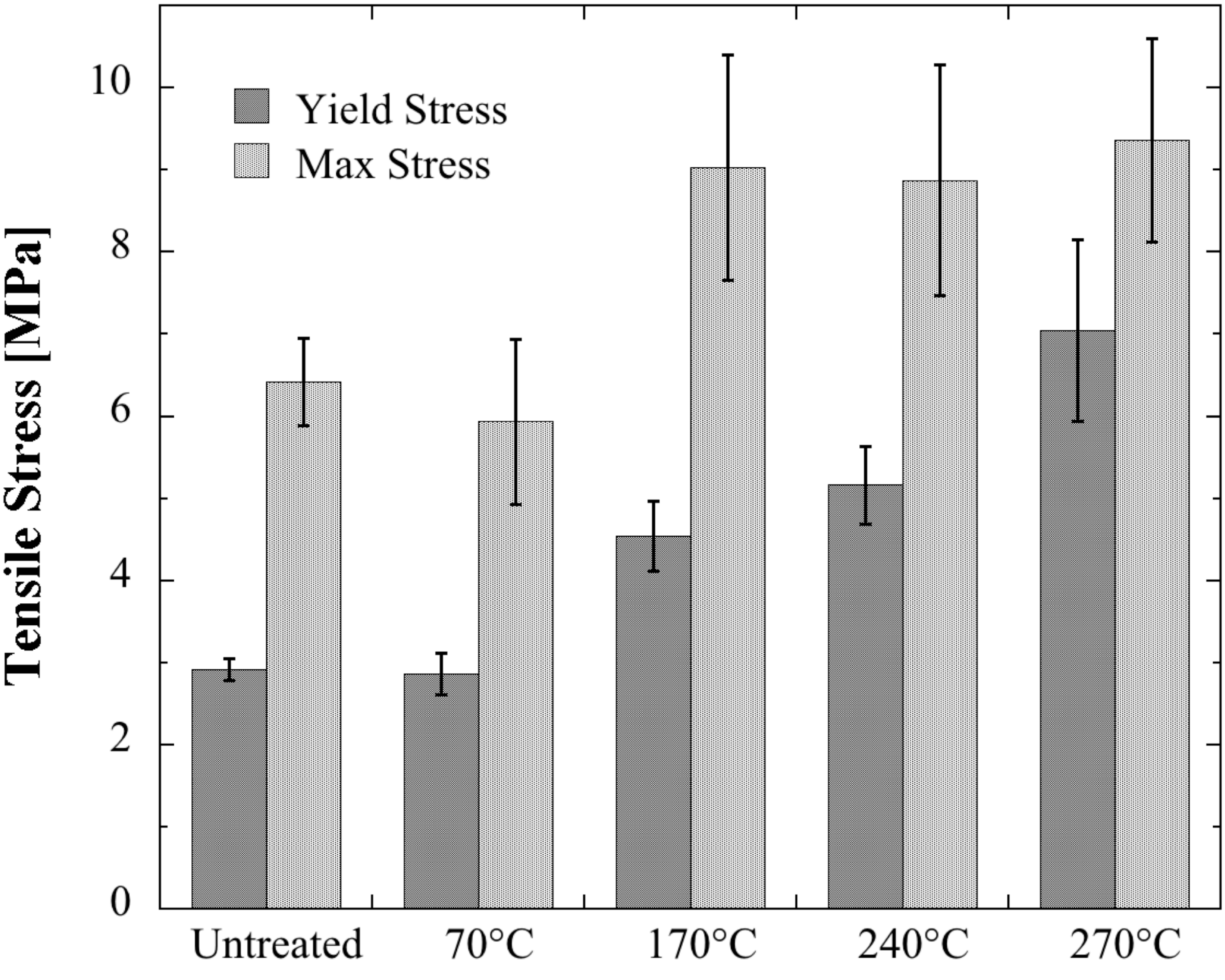

Figure 9. Plot of the yield stress and maximum (breaking) stress of PA 6,6 electrospun mats vs. annealing temperature.

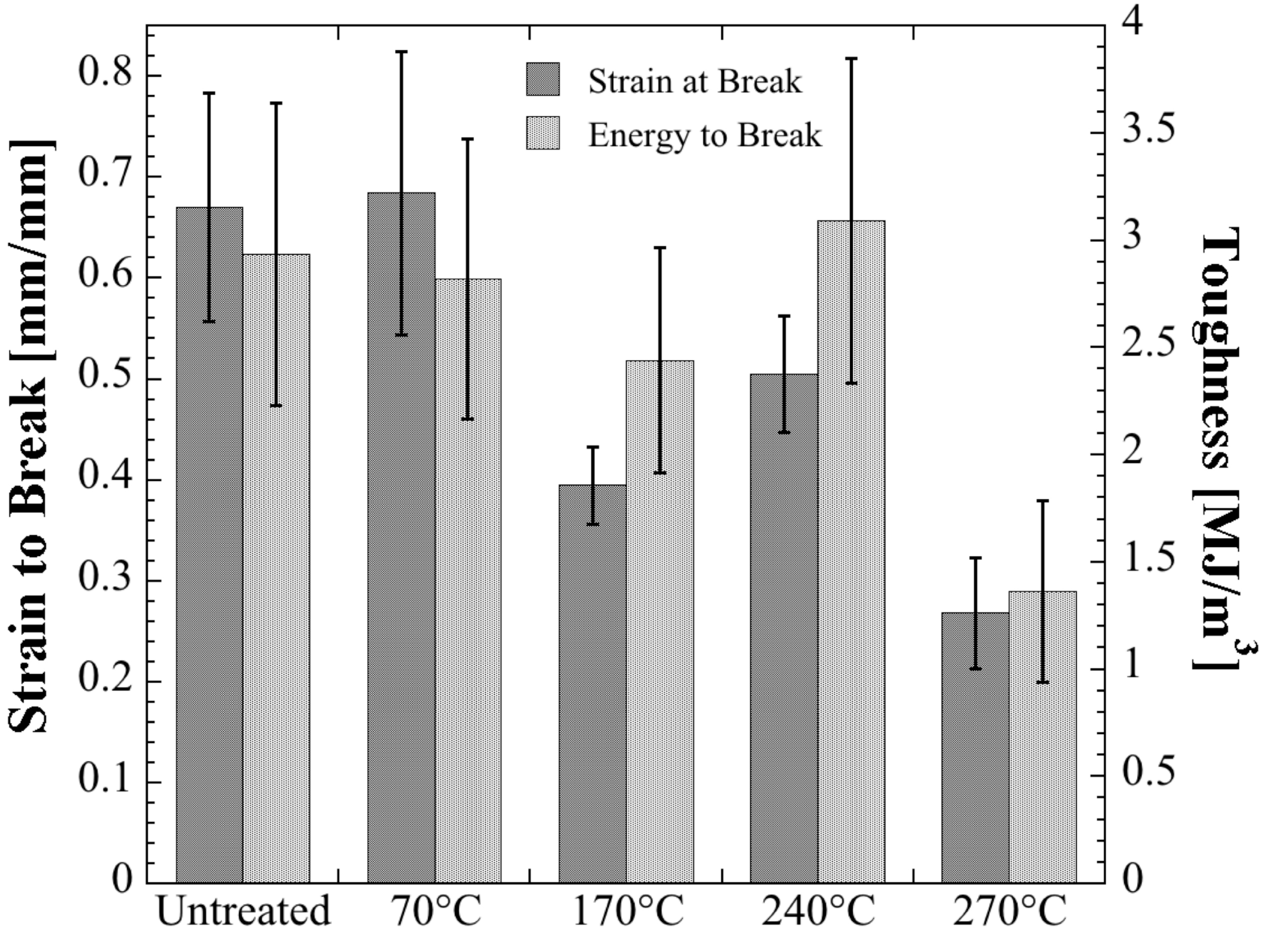

Figure 10. Plot of the strain-to-break and tensile energy-to-break (Toughness) vs. annealing temperature for PA 6,6 nanofiber mats.

3.4. Tribology of Electrospun Mats

Untreated electrospun fiber mats are typically fragile and susceptible to wear and delamination, even under conditions of gentle handling. This is a source of concern for the post-spin handling as well as the end-use of such mats, and could be a critical limitation to their service lifetime. To quantify the tribological behavior of nonwovens, the coefficient of friction (μ) was measured using a standardized testing material (Calibrade® H-38 abrasive wheel) for each of the fiber mats, as-spun and after each of the prescribed annealing temperatures. A plot of the friction force vs. the normal force for each annealing temperature is shown in Figure 11; from this plot, the friction coefficient can be determined by taking the ratio of the average measured friction force to the applied normal force. A plot of the coefficient of friction vs. the normal force is shown in Figure 12; note that there is a modest decrease in the coefficient of friction with increasing normal force at low loads, but that above 1.0 N (~100 g applied load), the friction coefficient becomes relatively constant for each sample. The decrease in coefficient of friction with increasing load is typical of compressible polymeric materials, whose shear strength increases with applied load [41]. Mean friction coefficients at 50 g load decreased from 0.97 for the as-spun mat to 0.85 for the 170 °C heat-treatment sample, to 0.69 for the 240 °C heat-treated mat. A lower mean coefficient of friction for the fiber mats is typically desirable, as it implies that the mat experiences smaller forces during abrasive contact with a counter-face, which could lead to significantly less wear.

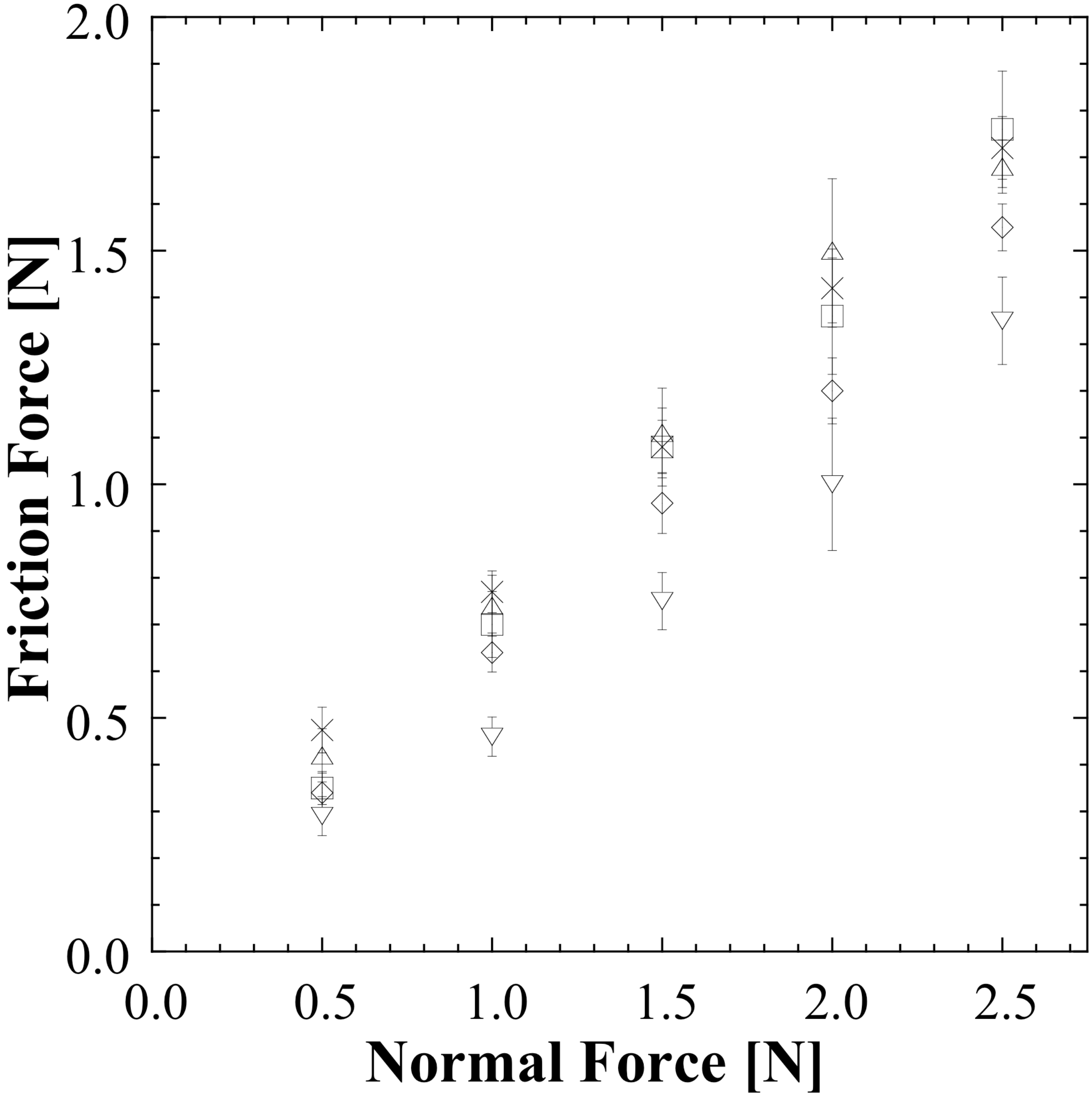

Figure 11. Friction force of PA 6,6 mats as a function of the normal force after annealing at various temperatures: as-spun (×), 70 °C (□), 170 °C (△), 240 °C (◇) and 270 °C (▽).

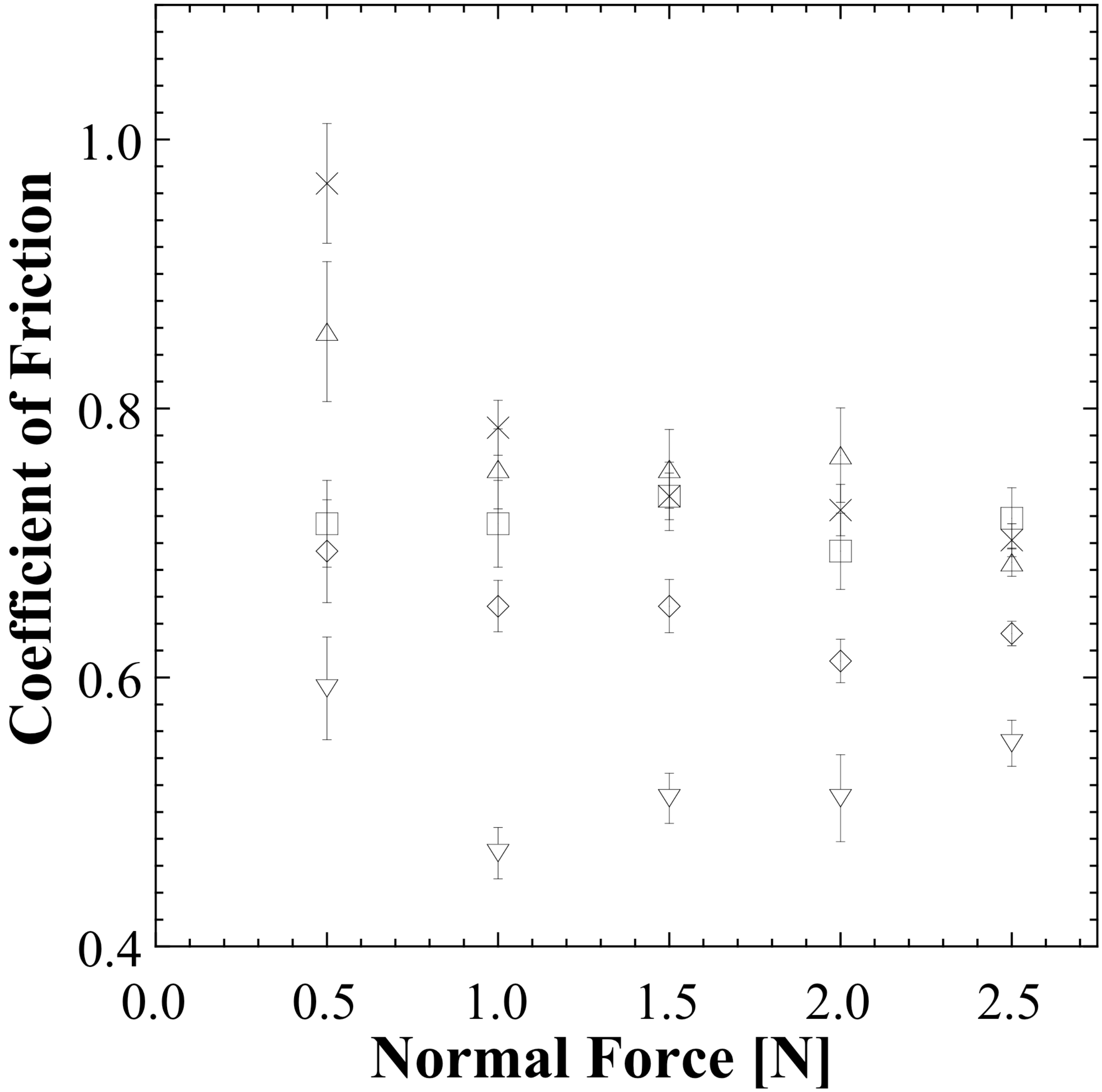

Figure 12. Coefficient of Friction of PA 6,6 mats as a function of the normal force after annealing at various temperatures: as-spun (×), 70 °C (□), 170 °C (△), 240 °C (◇) and 270 °C (▽).

The Taber abraser was used to provide uniform, low levels of abrasive wear in order to measure quantitatively the changes in the tribological response of annealed electrospun PA 6,6 fiber mats. The surface roughness of a material can be a major factor in the tribological response, relating to the area of contact between the test material and the abrasive counter-surface; all of the PA 6,6 mats used in these wear tests had a mean-value roughness (R_a) on the order of 1.5-2.5 μm; values are listed in Table 2. An applied load of 50 g was used for testing because it was sufficiently high to yield consistent coefficient of friction values, while being a low enough such that more than 100 abrasion cycles could be performed before destruction of each sample. Temperature changes to the fiber mat during abrasive cycling were monitored using a non-contact infrared thermometer. The surface temperature of the mats were measured to be 25.0 ± 0.2 °C before wear testing and typically did not increase by more than 0.4 °C (25.8 °C maximum reading) at any point during testing, even up to 500 continuous abrasion cycles. The mats never approached the T_g (45 °C) or T_m (254 °C) of the bulk PA 6,6 during testing and should therefore not have undergone any thermally induced transformations or deformations due to the wear cycling.

Visual inspection of the nonwoven membranes after 10, 50, and 100 abrasion cycles indicated significant qualitative differences in the wear mechanisms between the samples annealed at the various temperatures, as shown in Figure 13. The as-spun sample and the sample annealed at 70 °C exhibit some observable signs of deformation and wear after as few as 10 abrasion cycles, and significant levels of deformation and wear after 50 cycles; the samples typically reach tribological destruction (>50% of sample mass removed from the wear path) by approximately 100 abrasion cycles. The sample annealed at 170 °C exhibited only marginally more wear resistance; however, the mechanism of wear seems to have changed from a fibrous pulling/displacement-type deformation to more of a tearing and rolling mechanism. The sample annealed at 240 °C exhibited significantly more robust wear resistance, and shows only minor wear and abrasive tears at 10 and 50 cycles, before exhibiting more significant tearing and delamination after 100 cycles. The samples annealed at 240 °C do not reach the 50% mass loss wear destruction until as much as 500 abrasion cycles. The samples annealed at 270 °C were also very robust, showing minimal signs of wear until 50 abrasion cycles (most of which are small tears and holes), then exhibiting some more significant levels of tearing after 100 cycles.

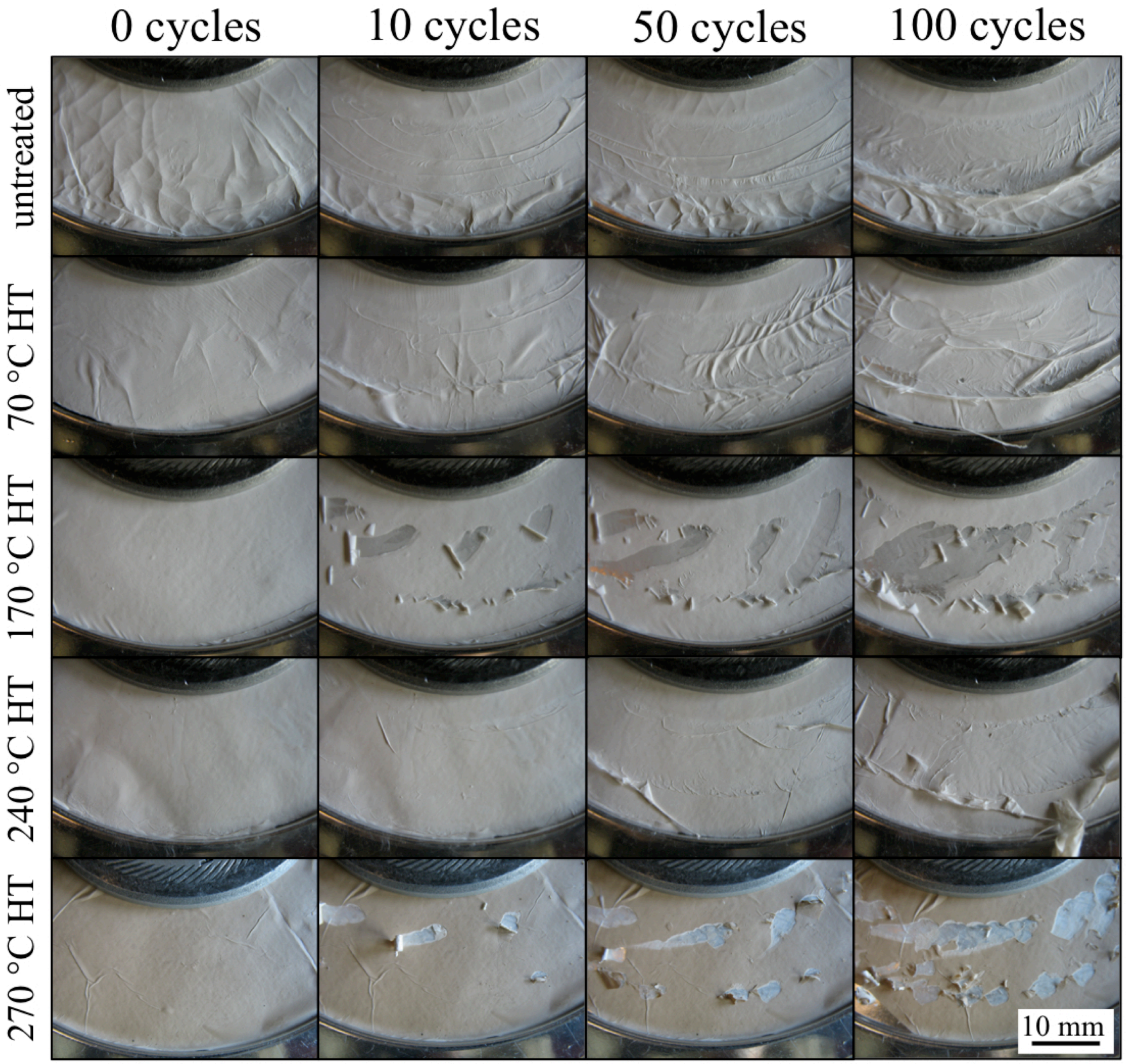

Figure 13. Optical images of abrasive wear path for fiber mats at 0, 10, 50, and 100 wear cycles under 50 g applied load (top row: as-spun; second row: 70 °C heat-treated; third row: 170 °C heat-treated, fourth row: 240 °C heat-treated, bottom row: 270 °C heat-treated), scale bar is 10 mm.

Quantitative evaluation of the abrasive wear properties of the electrospun PA 6,6 mats was performed by measuring the mass loss of the samples after a specified number of abrasion cycles. A plot of the abrasive mass loss vs. the number of cycles for 50 g applied load is shown in Figure 14 for 10, 50, 100, and 250 cycles. The wear rate was measured up to approximately 50% mass loss within the wear path, or ~35-40 mg for each sample, which was defined as the point of tribological destruction. Significantly more material was removed from the untreated electrospun mats compared to the thermally annealed samples, with the most wear-resistant mats being those annealed at 240 °C; this is consistent with what was observed qualitatively from visual inspection. Modest decreases in the effective wear rate of the electrospun fiber mats was observed with increasing temperature of thermal annealing for 70 °C, 170 °C, and 240 °C; however, annealing the PA 6,6 mats at 270 °C (above the T_m) yielded an increase in the wear rate compared to the mat annealed at 240 °C, indicating that there could be significant morphological changes in the samples annealed at 270 °C that affected the wear response. The effective wear rate for each sample was calculated as the slope of the tangent to a best-fit second-order polynomial to each set of wear data, evaluated at 100 cycles. The effective wear rate was seen to decrease from 8.10 x 10^6 g/cm for the as-spun PA 6,6 sample down to 3.01 x 10^6 g/cm for the mats annealed at 240 °C. The improvements to the wear resistance of electrospun PA 6,6 mats were not as significant as previously seen for poly(trimethyl hexamethylene terepthalamide) [PA 6(3)T] fiber mats [17]. However, the amorphous polyamide samples also had greater changes in mechanical properties with thermal annealing. A summary of all the tribological data including the mean-value roughness (R_a), mean coefficient of friction (μ), and effective wear rate are compiled in Table 2.

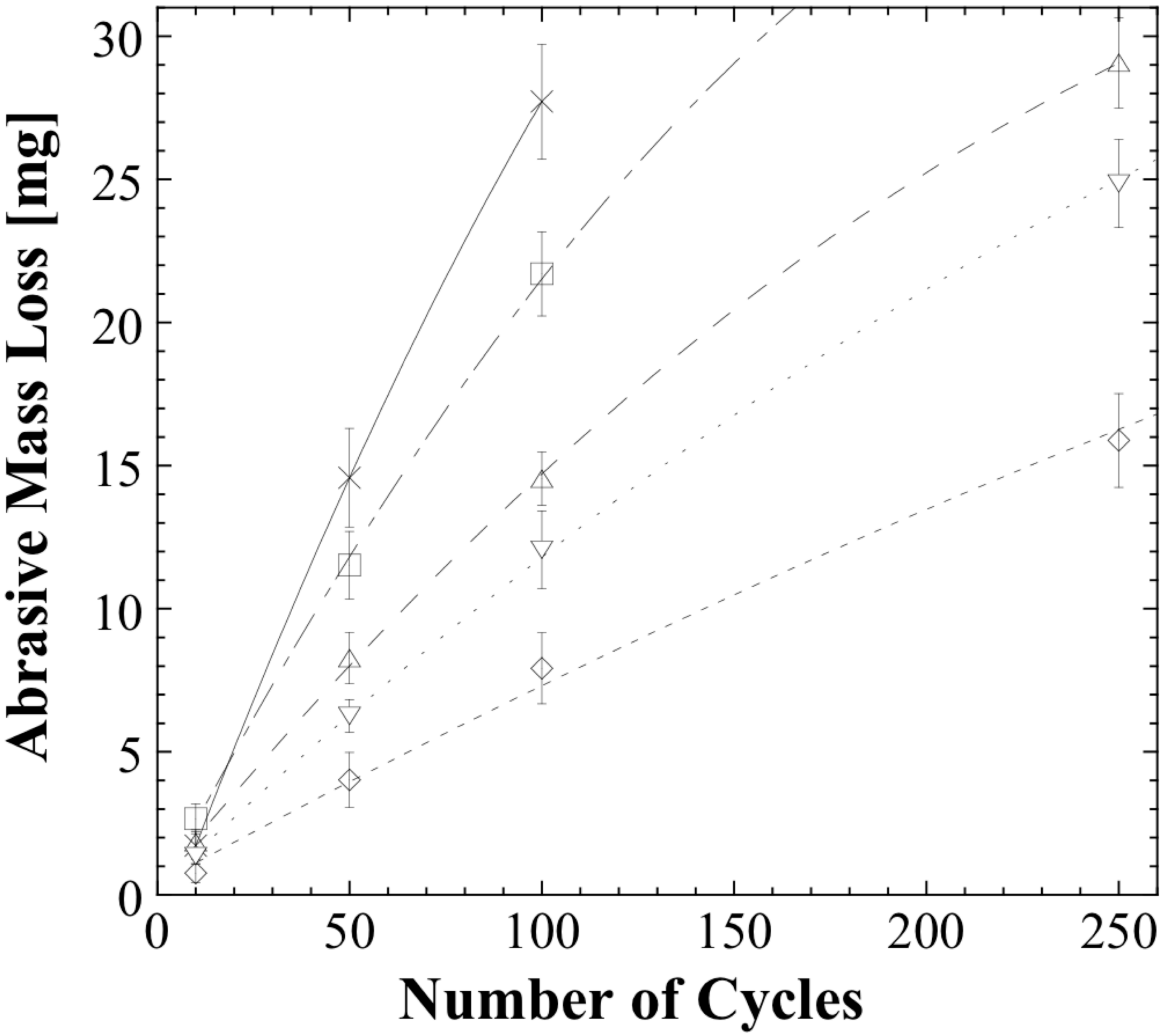

Figure 14. Abrasive mass losses of electrospun nanofiber mats as a function of the number of wear cycles under 50 g load: untreated (×), 70 °C heat-treated (□), 170 °C heat-treated (△), 240 °C heat-treated (◇) and 270 °C heat-treated mats (▽).

Table 2. Summary of Tribological Properties of PA 6,6 Nanofiber Mats

	R_a [µm]	Mean coefficient of friction, µ (50 g)	Wear rate (50g) [g/cm]
Untreated	2.459	0.97	8.10×10^{-6}
70 °C HT	1.887	0.71	7.12×10^{-6}
170 °C HT	2.298	0.85	5.17×10^{-6}
240 °C HT	2.145	0.69	3.01×10^{-6}
270 °C HT	1.581	0.59	4.55×10^{-6}

The tensile mechanical properties and the abrasive wear properties of polymeric materials tend to be strongly correlated. The deformation of a surface is generally a function of the indentation hardness, the relative motion opposed by the frictional force, and disruption of material at the contact points, involving an amount of work equal to the area under the stress-strain curve. One of the most commonly used correlations based on such a mechanism is the Ratner-Lancaster correlation [42,43], which predicts the wear rate, W, as:

$$W = C\left(\mu \frac{L}{H\sigma_b\varepsilon_b}\right) \tag{5}$$

where C is a constant, µ is the coefficient of friction, L is the applied load, H is the hardness, σ_b is the breaking stress of the material, and ε_b is the breaking strain. The indentation hardness of most polymer fiber mats is relatively small and does not change significantly between materials; therefore, the dominant parameters tend to be σ_b and ε_b [44,45]. For electrospun fiber mats, we have previously proposed that the breaking stress and breaking strain of individual fibers is reflected in the yield stress and strain of the nonwoven mats; based on this, a modified version of the Ratner-Lancaster relationship is obtained, in which the yield stress, σ_y, and yield strain, ε_y, of the mat replace the breaking stress and strain of the fibers [17]. The wear rate is furthermore put on a mass basis by the density of the polymer mat, ρ, to get:

$$W \propto \left(\frac{\rho\mu L}{\sigma_y\varepsilon_y}\right) \tag{6}$$

This modified Ratner-Lancaster relationship has been show to correlate well the wear results for the electrospun mats of the amorphous polyamide PA 6(3)T [17]. Figure 15 compares the effective wear rates of the treated PA 6,6 fiber mats to the modified Ratner-Lancaster wear rate relationship from equation 6, along with the previously reported PA 6(3)T data. The effective wear rate for the PA 6,6 mats increases proportionately with the quantity $(\rho\mu L)/(\sigma_y\varepsilon_y)$ for the samples annealed below the T_m.

Only the sample annealed at 270 °C exhibits a wear rate that deviates significantly from the proposed scaling. This deviation from the expected scaling of the wear rate is most likely due to morphological changes of the crystal structure within the fibers, which could significantly alter the fracture mode and breaking strain of the individual fibers. With the exception of the sample annealed above T_m (270 °C heat treatment), the semicrsytalline PA 6,6 electrospun nonwoven mats wear more slowly, by a factor of 2-3x, compared to the amorphous PA 6(3)T electrospun nonwoven mats. These results show that the mechanical and tribological properties of electrospun fiber mats are well-correlated by the modified Ratner-Lancaster model, and that the effects on wear resistance due to the crystallinity and crystal morphology within a semi-crystalline polymeric fiber mat cannot be neglected.

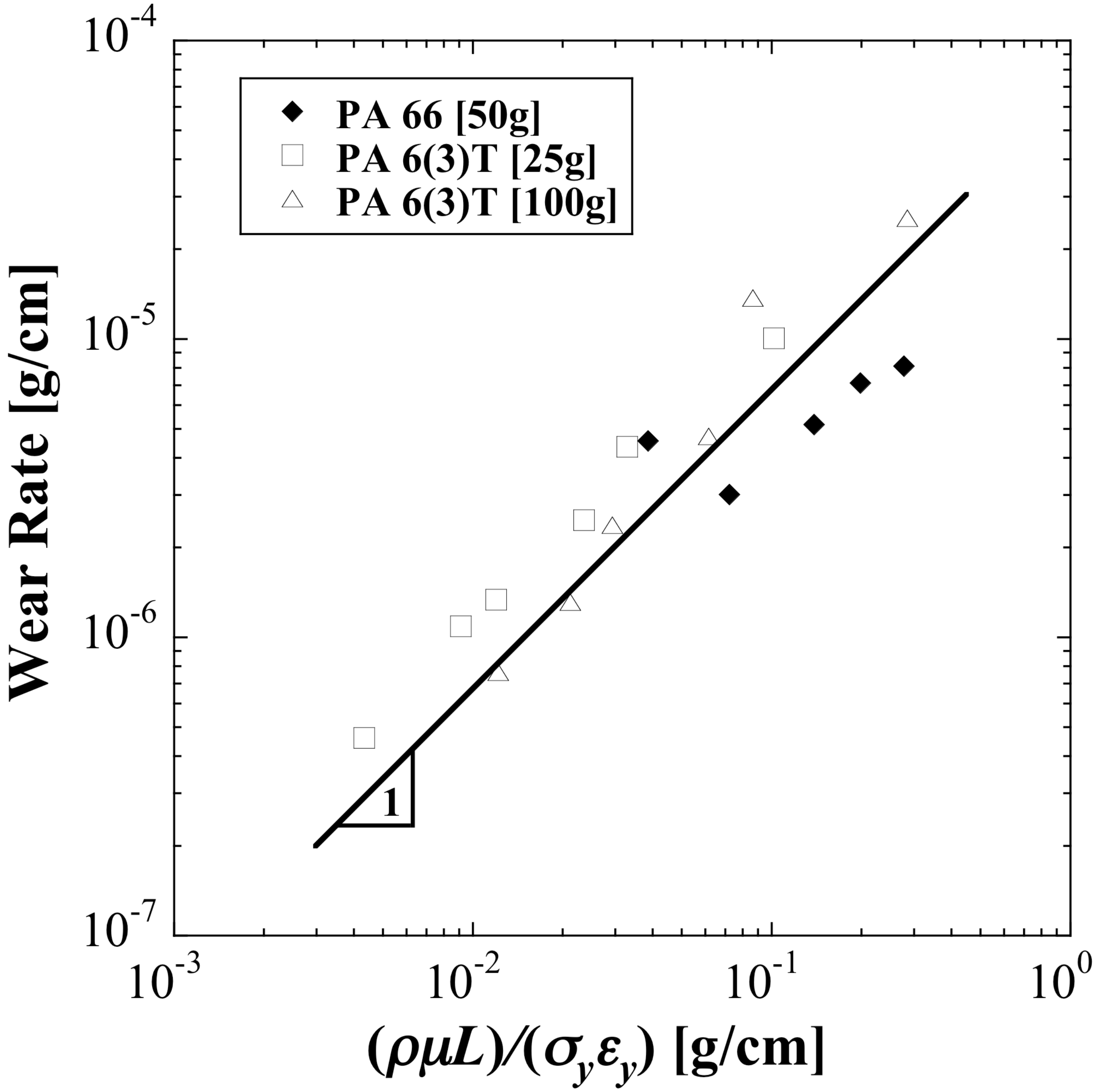

Figure 15. Effective wear rate vs. $(\rho\mu L)/(\sigma_y\varepsilon_y)$ of nanofiber mats subjected to varying temperatures of thermal treatment: PA 6,6 at 50 g applied load (◆) [this work], and PA 6(3)T from previous tribology investigation [17] at 25 g (□) and 100 g (△) applied load. The line with slope=1 is drawn as a guide to the eye.

4. Conclusions

The tribological and mechanical response of thermally annealed semi-crystalline electrospun PA 6,6 fiber mats were investigated in this work. The crystallinity of the fiber mats was observed to exhibit small changes as a function of the annealing temperature, with more pronounced increases to the percent crystallinity, according to WAXD, when samples were treated above T_B. Significant changes to the crystal morphology and orientation were observed within the PA 6,6 fibers as molecular alignment changed from parallel to the fiber axis to perpendicular for samples treated above T_B. The change in molecular orientation is most likely due to the initial strain alignment when forming the crystallites as a result of the jet stretching during the electrospinning process. During the thermal annealing process above T_B, the molecular orientation relaxes as the chains become more mobile. The Young's modulus, yield stress, and toughness of the nonwoven mats were found to change with an increase in the annealing temperature through the glass transition, Brill transition, and crystalline melting points, at the expense of mat porosity. The yield stress increased modestly from 2.9 MPa for the untreated PA 6,6 nanofiber mat, to 4.5 MPa for the 170 °C heat-treatment, without suffering a significant loss of porosity. The yield stress could then be increased further up to 7.1 MPa after 270 °C heat-treatment (above the T_m), at a substantial loss to the mat porosity (90% to 72%). In addition to gains in mechanical integrity, there was also an improvement in the wear resistance of the semi-crystalline electrospun fiber mats with thermal treatment. Annealing at 240 °C results in a significant decrease in the effective wear rate relative to that of the as-spun mats, from 8.10×10^{-6} g/cm to 3.01×10^{-6} g/cm at 50 g applied load, while the porosity decreases only modestly, from 90% to 86%. The mechanical and tribological properties of the thermally annealed PA 6,6 fiber mats were found to exhibit significant improvements through the Brill transition temperature, comparable to the improvements observed when annealing amorphous PA 6(3)T electrospun mats near the glass transition temperature. The effective wear rate of the electrospun PA 6,6 fiber mats was well-described by a modified Ratner-Lancaster relationship for wear rate of polymeric materials, $W \sim (\rho \mu L)/(\sigma_y \varepsilon_y)$ for samples annealed below the T_m, suggesting that the mechanism of wear is primarily due to the breakage of fibers that apparently contributes to yield in these nonwoven mats. Only the sample annealed at 270 °C exhibits a wear rate that deviated significantly from the proposed scaling. The deviation from the modified Ratner-Lancaster correlation is most likely due to the changes observed in the crystal orientation and morphology; these changes could affect the individual fiber properties such as the fracture mode and breaking strain of the individual fibers, resulting in a lower mechanical energy required to remove material from the surface. The mechanical and tribological properties of electrospun fiber mats are found to be inter-related, and the effects of crystallinity and crystal morphology within semi-crystalline polymeric fiber mats significant with respect to the wear resistance.

Acknowledgements

Funding for this work was provided by the U.S. Army through the Institute for Soldier Nanotechnologies (ISN) under AROW911NF-07-D-0004. The authors would like to thank Prof. Stephen Burke Driscoll and the Plastics Engineering Department at the University of Massachusetts Lowell for use of their Taber abraser and for discussions about wear testing of textiles. The authors would like to thank Dr. Jason Lee for his assistance with X-ray diffraction and Tim McClure for his assistance with FTIR. The authors would also like to acknowledge the Hammond lab at MIT for use of their Dektak surface profiling system, and the MIT Institute of Soldier Nanotechnology and Center for Materials Science and Engineering (CMSE) for use of facilities.

References

---

[1] J. Doshi, D.H. Reneker, Electrospinning process and applications of electrospun fibers, Journal of Electrostatics 35 (1995) 151-160.

[2] Y.M. Shin, M.M. Hohman, M.P. Brenner, G.C. Rutledge, Electrospinning: a whipping fluid jet generates submicron polymer fibers, Applied Physics Letters 78 (2001) 1149-1151.

[3] R.G. Flemming, C.J. Murphy, G.A. Abrams, S.L. Goodman, P.F. Nealey, Effects of synthetic micro- and nano-structured surfaces on cell behavior, Biomaterials 20 (1999) 573-588.

[4] J.A. Matthews, G.E. Wnek, D.G. Simpson, G.L. Bowlin, Electrospinning of collagen nanofibers, Biomacromolecules 3 (2002) 232-238.

[5] K. Kim, M. Yu, X. Zong, J. Chiu, D. Fang, Y.-S. Seo, B.S. Hsiao, Control of degradation rate and hydrophilicity in electrospun non-woven poly (D, L-lactide) nanofiber scaffolds for biomedical applications, Biomaterials 24 (2003) 4977-4985.

[6] J. Zeng, X. Xu, X. Chen, Q. Liang, X. Bian, L. Yang, X. Jing, Biodegradable electrospun fibers for drug delivery, Journal of Controlled Release 92 (2003) 227-231.

[7] X.Y. Wang, C. Drew, S.H. Lee, K.J Senecal, J. Kumar, L.A. Samuelson, Electrospinning technology: A novel approach to sensor application, Journal of Macromolecular Science-Pure and Applied Chemistry A39 (2002) 1251-58.

[8] J. Choi, K.M. Lee, R. Wycisk, P.N. Pintauro, P.T. Mather, Nafion-impregnated electrospun polyvinylidene fluoride composite membranes for direct methanol fuel cells, Journal of Power Sources 180 (2008) 167-171.

[9] R. Bajon, S. Balaji, S.M. Guo, Electrospun Nafion Nanofiber for Proton Exchange Membrane Fuel Cell Application, Journal of Fuel Cell Science Technology 6 (2009) 031004.

[10] L. Li, L.M. Bellan, H.G. Craighead, M.W. Frey, Formation and properties of nylon-6 and nylon-6/montmorillonite composite nanofibers, Polymer 47 (2006) 6208-6217.

[11] C.L. Pai, M.C. Boyce, G.C. Rutledge, Mechanical properties of individual electrospun PA 6 (3) T fibers and their variation with fiber diameter, Polymer 52 (2011) 2295-2301.

[12] H.J. Jin, H.S. Chen, V. Karageorgiou, G.H. Altman, D.L. Kaplan, Human bone marrow stromal cell responses on electrospun silk fibroin mats, Biomaterials 25 (2004) 1039-1047.

[13] X.H. Zong, S.F. Ran, D.F. Fang, B.S. Hsiao, B. Chu, Control of structure, morphology and property in electrospun poly (glycolide-*co*-lactide) non-woven membranes via post-draw treatments, Polymer 44 (2003) 4959-4967.

[14] G.C. Engelmayr Jr, M.S. Sacks, A structural model for the flexural mechanics of nonwoven tissue engineering scaffolds, Journal of Biomechanical Engineering 128 (2006) 610-622.

[15] C.L. Pai, M.C. Boyce, G.C. Rutledge, On the importance of fiber curvature to the elastic moduli of electrospun nonwoven fiber meshes, Polymer 52 (2011) 6126-6133.

[16] X. Wang, K. Zhang, M. Zhu, B.S. Hsiao, B. Chu, Enhanced mechanical performance of self-bundled electrospun fiber yarns via post-treatments, Macromolecular Rapid Communications 29 (2008) 826-831.

[17] M.M. Mannarino, G.C. Rutledge, Mechanical and tribological properties of electrospun PA 6 (3) T fiber mats, Polymer 53 (2012) 3017-3025.

[18] C. Lai, G. Zhong, Z. Yue, G. Chen, L. Zhang, A. Vakili, Y. Wang, L. Zhu, J. Liu, H. Fong, Investigation of post-spinning stretching process on morphological, structural, and mechanical properties of electrospun polyacrylonitrile copolymer nanofibers, Polymer 52 (2011) 519-528.

[19] H. Na, Y. Zhao, C. Zhao, C. Zhao, X. Yuan, Effect of hot‐press on electrospun poly(vinylidene fluoride) membranes, Polymer Engineering And Science 48 (2008) 934-940.

[20] L. Jeong, K.Y. Lee, J.W. Liu, W.H. Park, Time-resolved structural investigation of regenerated silk fibroin nanofibers treated with solvent vapor, International Journal of Biological Macromolecules 38 (2006) 140-144.

[21] C.L. Pai, M.C. Boyce, G.C. Rutledge, Morphology of porous and wrinkled fibers of polystyrene electrospun from dimethylformamide, Macromolecules 42 (2009) 2102-2114.

[22] S. Derler, G.U. Schrade, L.C. Gerhardt, Tribology of human skin and mechanical skin equivalents in contact with textiles, Wear 263 (2007) 1112-1116.

[23] L.C. Gerhardt, N. Mattle, G.U. Schrade, N.D. Spencer, S. Derler, Study of skin-fabric interactions of relevance to decubitus: friction and contact-pressure measurements, Skin Research and Technology 14 (2007) 77-88.

[24] Y. Liu, L. Cui, F. Guan, Y. Gao, N.E. Hedin, L. Zhu, H. Fong, Crystalline morphology and polymorphic phase transitions in electrospun nylon-6 nanofibers, Macromolecules 40 (2007) 6283-6290.

[25] E. Zussman, M. Burman, A.L. Yarin, R. Khalfin, Y. Cohen, Tensile deformation of electrospun nylon-6,6 nanofibers, Journal of Polymer Science Part B-Polymer Physics 44 (2006) 1482-1489.

[26] K. Gao, X. Hu, C. Dai, T. Yi, Crystal structures of electrospun PVDF membranes and its separator application for rechargeable lithium metal cells, Materials Science & Engineering B 131 (2006) 100-105.

[27] D. Cho, E. Zhmayev, Y.L. Joo, Structural studies of electrospun nylon 6 fibers from solution and melt, Polymer 52 (2011) 4600-4609.

[28] W. He, Z.W. Ma, T. Yong, W.E. Teo, S. Ramakrishna, Fabrication of collagen-coated biodegradable polymer nanofiber mesh and its potential for endothelial cells growth, Biomaterials 26 (2005) 7606-7615.

[29] X. Zhu, W. Cui, X. Li, Y. Jin, Electrospun fibrous mats with high porosity as potential scaffolds for skin tissue engineering, Biomacromolecules 9 (2008) 1795-1801.

[30] H.W. Starkweather, P. Zoeller, G.A. Jones, The heat of fusion of 66 nylon, Journal of Polymer Science: Polymer Physics 22 (1984) 1615-1621.

[31] M. Wang, J.H. Yu, D.L. Kaplan, G.C. Rutledge, Production of submicron diameter silk fibers under benign processing conditions by two-fluid electrospinning, Macromolecules 39 (2006) 1102-1107.

[32] S.J. Cooper, M. Coogan, N. Everall, I. Priestnall, A polarized μ-FTIR study on a model system for nylon 6,6: implications for the nylon Brill structure, Polymer 42 (2001) 10119-10132.

[33] N.S. Murty, M. Stamm, J.P. Sibilia, S. Krimm, Structural-changes accompanying hydration in nylon-6, Macromolecules 22 (1989) 1261-1267.

[34] N.Y. Jia, H.A. Frenkel, V.A. Kagan, Effects of moisture conditioning methods on mechanical properties of injection molded nylon 6, Journal of Reinforced Plastics and Composites 23 (2004) 729-737.

---

[35] D.-J. Lin, C.-L. Chang, C.-K. Lee, L.-P. Cheng, Fine structure and crystallinity of porous Nylon 66 membranes prepared by phase inversion in the water/formic acid/Nylon 66 system, European Polymer Journal 42 (2006) 356-367.

[36] C.W. Bunn, E.V. Garner, The crystal structures of two polyamides ('nylons'), Proceedings of the Royal Society of London A 189 (1947) 39-68.

[37] H.W. Starkweather, G.A. Jones, Crystalline transitions in powders of nylon 66 crystallized from solution, Journal of Polymer Science: Polymer Physics Edition 19 (1981) 467-477.

[38] N.S. Murthy, S.A. Curran, S.M. Aharoni, H. Minor, Premelting crystalline relaxations and phase transitions in nylon 6 and 6, 6, Macromolecules 24 (1991) 3215-3220.

[39] C. Ramesh, A. Keller, S.J.E.A. Eltink, Studies on the crystallization and melting of nylon-6,6: 1. The dependence of the Brill transition on the crystallization temperature, Polymer 35 (1994) 2483-2487.

[40] N. Vasanthan, Crystallinity determination of nylon 66 by density measurement and fourier transform infrared (FTIR) spectroscopy, Journal of Chemical Education 89 (2012) 387-390.

[41] N.P. Suh, Tribophysics, 1st ed. New Jersey: Prentice-Hall, 1986.

[42] K.G. Budinski, Resistance to particle abrasion of selected plastics, Wear 203 (1997) 302-309.

[43] J.K. Lancaster, Abrasive wear of polymers, Wear 14 (1969) 223-239.

[44] A. Wang, D.C. Sun, C. Stark, J.H. Dumbleton, Wear mechanisms of UHMWPE in total joint replacements, Wear 181 (1995) 241-249.

[45] P.H. Shipway, N.K. Ngao, Microscale abrasive wear of polymeric materials, Wear 255 (2003) 742-750.